Advances in Water Resources 86 (2015) 14–31

Contents lists available at ScienceDirect

Advances in Water Resources

journal homepage: www.elsevier.com/locate/advwatres

Benchmarking a multiresolution discontinuous Galerkin shallow water model: Implications for computational hydraulics

Daniel Caviedes-Voullième, Georges Kesserwani*

Pennine Water Group, Dept. of Civil and Structural Engineering, University of Sheffield, UK

ARTICLE INFO

Article history:
Received 10 April 2015
Revised 14 September 2015
Accepted 21 September 2015

Keywords:
Shallow water equations
Discontinuous Galerkin
Multiwavelets
Mesh adaptivity
Automated multiresolution modelling
Practical considerations

ABSTRACT

Numerical modelling of wide ranges of different physical scales, which are involved in Shallow Water (SW) problems, has been a key challenge in computational hydraulics. Adaptive meshing techniques have been commonly coupled with numerical methods in an attempt to address this challenge. The combination of MultiWavelets (MW) with the Runge–Kutta Discontinuous Galerkin (RKDG) method offers a new philosophy to readily achieve mesh adaptivity driven by the local variability of the numerical solution, and without requiring more than one threshold value set by the user. However, the practical merits and implications of the MWRKDG, in terms of how far it contributes to address the key challenge above, are yet to be explored. This work systematically explores this, through the verification and validation of the MWRKDG for selected steady and transient benchmark tests, which involves the features of real SW problems. Our findings reveal a practical promise of the SW-MWRKDG solver, in terms of efficient and accurate mesh-adaptivity, but also suggest further improvement in the SW-RKDG *reference scheme* to better intertwine with, and harness the prowess of, the MW-based adaptivity.

1. Introduction

Godunov-type [21] Shallow Water (SW) models are well-recognised for incorporating the widest range of flow transitions within the numerical discretization. They have undergone significant developments over the past few decades and lie at the heart of the latest hydraulic modelling packages [15,23,47,60].

Most commonly, Godunov-type Finite Volume (FV) SW models are built on the assumption that each discrete control volume is *local* piecewise-constant information to the conservative form of the Shallow Water Equations (SWE). Connecting local information across inter-elemental faces, via the spatial fluxes obtained from the solution of Riemann Problems, is achieved to evolve the information in time [66]. In this sense, a FV formulation is first-order accurate, or may be said to allow single-scale of *local* accuracy and resolution. High order variants have been proposed (e.g. MUSCL [27,50,63], PPM [12] and WENO [41,54,69]) using *non-local* reconstruction of polynomial estimates from the *local* piecewise-constant information. However, they dictate widening of the calculation stencil, which thereby requires information from *non-local* neighbour cells; thus removing the essence of the *locality* featuring in the first-order FV formulation. Practically, such non-locality complicates the handling key features (e.g. treatment of terrain datasets, moving wet-dry zones and boundary conditions [26] and the exploitation of parallel computing efficiency; this may be a key reason why usable and parallelized Godunov-type SW models are most often first-order accurate [4,7,13,29,40,47].

The Runge–Kutta (RK) Discontinuous Galerkin (DG) method has risen as a viable alternative to enable high-order accuracy within the spirit of the local FV Godunov-type foundation. The RKDG formulation locally shapes and evolves (from conservation principles) piecewise-polynomial solutions, or local data-sets of information [11]. It has become increasingly adopted and improved for SW modelling [16,37,64,68,73], and has been demonstrated to offer numerous benefits (e.g. higher-quality solution behaviour on very coarse meshes, improved velocity predictions and increased local accuracy for wet-dry front tracking [30,35,37]. Nonetheless, the amount of local information needed (i.e. for storage and evolution of polynomial coefficients) depends on the accuracy-order, the spatial dimensionality and spatial resolution. Proportional to these factors, the complexity of the RKDG formulation drastically increases as well as its computational and runtime costs. Consequently, RKDG SW models are most commonly second-order (RKDG2) and at most third-order (RKDG3).

In line with the development of robust and stable SW Godunov-type models, research efforts have also been active in attempting

* Corresponding author. Tel.: +441142225746.
E-mail addresses: d.caviedes@sheffield.ac.uk (D. Caviedes-Voullième), g.kesserwani@sheffield.ac.uk (G. Kesserwani).

http://dx.doi.org/10.1016/j.advwatres.2015.09.016

to accommodate the variability, multiplicity and inter-connectivity of the local spatial-resolutions that are involved in SW problems. Adaptive meshing techniques have become well-recognised as an optimal solution for the trade-off between spatial-resolution and computational cost [9,14,34,36,38,52,62]. However, conventional meshing techniques – coupled with either the FV or the DG formulation – are still hampered by many issues. The most relevant of them is generation of excessive error dissipation, nonphysical oscillation and loss of conservation [14,34,43,56,71]. Even for 1D SW modelling, explicit modification within a conventional adaptive mesh technique is required to ensure well-balanced numerical predictions at the same level of reliability of those predicted on the uniform mesh counterpart [14]. Similar problems have been reported when an adaptive SW model is faced with wetting and drying, and for the 2D case considering both (structured) quadrilateral and (unstructured) triangular meshes [43,71]. Generally, conventional adaptive mesh methods: (a) do not offer the option to control how much perturbation, in accuracy, is allowed relating to a reference scheme on a fine-uniform-mesh, (b) need separate parameters and criteria for treating mesh-coarsening and mesh-refinement processes, and (c) impose relatively fine baseline coarse resolution [34,51]. Therefore, this work is motivated by the further need to explore a more rigorous and integrated notion of mesh adaptivity in addressing the aforediscussed challenges.

Multiresolution analysis, spawning from applications in signal processing and image compression has been proposed for controlling mesh adaptivity in the context of solving PDEs and ODEs [2,24,46,61]. To achieve this in the framework of a local RKDG polynomial approximation, multiwavelets (MW) [1] offer a sound mechanism for transforming the single-resolution polynomial information into multiresolution information. The MW information comes into play as a key component of the encoded difference across two successive resolution levels. Hovhannisyan et al. [28] explored in detail how the combination of MW and the RKDG method (MWRKDG) is conceptually achieved in solving 1D scalar (hyperbolic) conservation laws. Their numerical analysis shows that the MW's scalability allows (i) a solution-driven mesh adaptation process controlled by one threshold-value parameter set in by the user, (ii) to quantitatively control the perturbation-error of the adaptive solution from its underlying uniform mesh solution (so-called *reference scheme*), and (iii) a choice for the threshold-value parameter so that the perturbation error does not exceed the discretization-error of the reference scheme on the finest grid accessible. Gerhard and Müller [20], Gerhard et al. [19] extended further the MWRKDG theory for more general inviscid hyperbolic conservation laws, including the 2D case. These works mainly studied strategies for the choice of the threshold-value in relation to the MW-based adaptivity, while remaining within the scope of solving homogeneous conservation laws.

In the context of SW modelling, the MWRKDG theory is little explored, to date, and requires further consideration to integrate the topography and friction source terms. Kesserwani et al. [31] presented a 1D SW-MWRKDG3 model based on a well-balanced 1D RKDG3 reference scheme [33]. Their results demonstrate that the features of the 1D RKDG3 scheme (i.e. well-balanced property and local slope limiting) are genuinely transferable to the adaptive setting of MWRKDG. A 2D SW-MWRKDG3 has been studied by [18] based on the reference 2D RKDG3 scheme of [70]. Their work theoretically proved that the SW-MWRKDG3 model delivers adaptive mesh simulations at the same level of confidence offered by the 2D RKDG3 reference scheme, in particular for the mass-conservation quantity. In both papers [18,31], a convergence analysis was carried out indicating that the *adaptivity* of the SW-MWRKDG model can simultaneously address challenges (a)–(c). Practically speaking, however, the SW-MWRKDG3 model [18] could not be assessed for realistic hydraulic tests, due to new conflicts identified between the choice of the reference RKDG3 reference scheme and adaptivity. One of these is stability conflicts when the wet-dry front is not (exactly) located at a cell interface, which is not ideal for adaptivity, notwithstanding that RKDG3 models are harder to stabilise. Consequently, the deployment of more appropriate reference RKDG2 schemes remains a key issue in order to be able to explore and exploit the adaptivity of MWRKDG for practical SW modelling.

This paper aims to offer new insights into the response of the MWRKDG adaptivity for practical SW simulations. Two adaptive SW-MWRKDG2 models are used for solving the SWE with friction and topography source terms, and with presence of wetting and drying. The adaptive models are tailored and studied based on two reference RKDG2 schemes: the scheme in [36] and the one in [70]. The SW-MWRKDG2 models are exhaustively tested for three hydraulic benchmarks, and then assessed in replicating dam-break flow experiments. The performances of the SW-MWRKDG2 models are analysed in detail, and compared (when possible) along with a SW-MWRKDG3 model results considering subjects of: stability for SW modelling, adaptivity response to the features of the reference scheme, and operational and runtime saving.

2. Shallow water model

The 1D shallow water equations, per unit width, can be written as

$$\frac{\partial \mathbf{U}(x,t)}{\partial t} + \frac{\partial \mathbf{F}(\mathbf{U})}{\partial x} = \mathbf{S}(\mathbf{U},x) \tag{1}$$

where $\mathbf{U}(x,t)$ is the vector of conserved variables

$$\mathbf{U} = [h, q]^\top \tag{2}$$

with h the water depth [L], $q = hu$ the unit discharge [L^2/T] and u the velocity [L/T].

The flux $\mathbf{F}(\mathbf{U})$ in Eq. (1) is

$$\mathbf{F}(\mathbf{U}) = \left[q,\ \frac{q^2}{h} + \frac{gh^2}{2}\right]^\top \tag{3}$$

The source term can include a number of different physical phenomena, but here it is restricted to bed and friction terms

$$\mathbf{S}(\mathbf{U},x) = \mathbf{B}(\mathbf{U},x) + \mathbf{H}(\mathbf{U},x) \tag{4}$$

where $\mathbf{B}(\mathbf{U},x)$ is the bed source term

$$\mathbf{B}(\mathbf{U},x) = \left[0, -gh\frac{\partial z}{\partial x}\right]^\top \tag{5}$$

with z the bed elevation [L] and g the acceleration of gravity [L/T^2]. Finally, $\mathbf{H}(\mathbf{U},x)$ is the friction source term

$$\mathbf{H}(\mathbf{U},x) = [0, -gh\sigma]^\top \tag{6}$$

in terms of the friction slope σ for which Manning's model is used

$$\sigma = \frac{n_\sigma^2 u|u|}{h^{4/3}} \tag{7}$$

with n_σ the Glaucker–Manning coefficient [$TL^{-1/3}$].

In order for the problem to be well-posed, it is of course necessary to supplement the equations with initial data $\mathbf{U}(x, t=0)$ and appropriate boundary conditions.

3. Discontinuous Galerkin framework

Consider Eq. (1), which is a system of non-homogeneous conservation laws. By multiplying the equation with a test function $\underset{\sim}{\nu}$, integrating by parts and making use of Gauss' theorem, the weak formulation for a 1D control volume is obtained

$$\int \frac{\partial \underset{\sim}{\mathbf{U}}}{\partial t}\underset{\sim}{\nu}\,dx - \int \mathbf{F}(\underset{\sim}{\mathbf{U}})\frac{\partial \underset{\sim}{\nu}}{\partial x}\,dx + \sum_\omega \tilde{\mathbf{F}}(\underset{\sim}{\mathbf{U}}_\omega^+, \underset{\sim}{\mathbf{U}}_\omega^-)\mathbf{n}_\omega \underset{\sim}{\nu}_\omega = \int \mathbf{S}(\underset{\sim}{\mathbf{U}},x)\underset{\sim}{\nu}\,dx$$

(8)

where $\underset{\sim}{\mathbf{U}}$ is an approximate solution to $\mathbf{U}$, $\tilde{\mathbf{F}}$ is the numerical flux obtained from the discontinuous solution at both sides ($^+$ and $^-$) of the edges ω of the control volume, $\mathbf{n}_\omega$ is the outer-pointing normal vector to the edges, i.e., $\mathbf{n}_\omega = \{-1, 1\}$ and $\underset{\sim}{\varphi}_\omega$ is the test function evaluated at cell edge ω.

The discontinuous Galerkin approximation assumes that the approximate solution is a modal decomposition which satisfies

$$\underset{\sim}{\mathbf{U}}_i = \sum_{k=0}^{p} \mathbf{U}_{i,k}\varphi_{i,k} \tag{9}$$

where $\varphi_{i,k}$ are polynomial basis functions locally supported on cell i, with polynomial degree $0 \leq k \leq p$, and $\mathbf{U}_{i,k}$ are time-dependent coefficients associated to each polynomial degree in cell i and are initialised in time level $n = 0$ as

$$\mathbf{U}^0_{i,k} = \int \mathbf{U}^0 \varphi_{i,k}\, dx \tag{10}$$

These coefficients are to be evolved in time, therefore they may be termed as degrees-of-freedom of the solution. The approximation in Eq. (9) has an order of accuracy $P = p + 1$. Therefore, if linear basis functions ($p = 1$) are used, second-order ($P = 2$) accuracy is achieved, and in consequence the scheme is referred to as DG2.

Let the test functions $\underset{\sim}{\varphi}$ be the set of basis functions $\{\varphi_{i,k}\}$, and the basis functions to be taken as Legendre polynomials

$$\varphi_k(\chi) = \frac{1}{2^k k!}\frac{d^k}{d\chi^k}(\chi^2 - 1)^k \tag{11}$$

which are scaled and shifted from their reference domain $\chi \in [-1, 1]$ into the local cell i defined by $x \in [x_{i-1/2}, x_{i+1/2}] = [x_i - \delta x_i/2, x_i + \delta x_i/2]$. They are also normalised, so that they are not only orthogonal but *orthonormal* in L^2, which is convenient for the adaptive strategy presented later on (but not a requirement of the reference DG scheme). Then, the scaled, shifted and normalised Legendre polynomials are

$$\varphi_{i,k}(x) = \sqrt{\frac{2}{2k+1}}\varphi_k\left(2\frac{x - x_i}{\delta x_i}\right) \tag{12}$$

where δx_i is the cell size. Then, using the *orthogonality* property of the Legendre polynomials it is possible to obtain the *evolution equation* for each of the degrees-of-freedom $\mathbf{U}_{i,k}$

$$\frac{\partial \mathbf{U}_{i,k}}{\partial t} = \underbrace{\int \mathbf{F}(\underset{\sim}{\mathbf{U}})\frac{\partial \varphi_{i,k}}{\partial x}\, dx}_{\mathcal{K}_{i,k}} - \underbrace{\sum_\omega \tilde{\mathbf{F}}(\underset{\sim}{\mathbf{U}}^+_\omega, \underset{\sim}{\mathbf{U}}^-_\omega)\mathbf{n}_\omega \varphi_{i,k,\omega}}_{\tilde{\mathcal{F}}_{i,k}} + \underbrace{\int \mathbf{S}(\underset{\sim}{\mathbf{U}}, x)\varphi_{i,k}\, dx}_{\mathcal{S}_{i,k}} \tag{13}$$

$\mathcal{K}_{i,k}$ are (volume) integrals of internal fluxes, $\tilde{\mathcal{F}}_{i,k}$ the (surface) integrals of the numerical fluxes and $\mathcal{S}_{i,k}$ the (volume) integrals of the source term.

Numerical fluxes $\tilde{\mathbf{F}}$ in Eq. (13) are obtained by approximately solving Riemann problems at the cell edges using Roe's linearization [57], i.e., Roe numerical flux. The source term is approximated by $\mathbf{S}(\underset{\sim}{\mathbf{U}}, x)$, which requires the existence of a bed $\underset{\sim}{z}$ projected onto the same orthonormal basis that define the DG discretization space, that is

$$\underset{\sim}{z} = \int z\varphi_{i,k}\, dx \tag{14}$$

However, to properly treat the source terms, the construction of this bed projection is further discussed in the next section.

The integrals in Eq. (13) are then computed numerically by appropriate Gauss quadrature rules that suit the polynomial degree of the integrand [10]. For $p = 1$, 2-point quadrature rules suffice for volume integrals. For $p = 2$, 4-point quadrature rules are used.

Integration in time is done by a strong stability preserving Runge–Kutta procedure [22], with two stages for RKDG2, and three stages for RKDG3.

3.1. Selected reference schemes

To complete the numerical scheme, several issues must be addressed. From the shallow water modelling perspective well-balancing strategy and depth-positivity must be ensured, as widely recognised in the FV [3,47,53,72] and DG [36,67] literature. Furthermore, from the high-order RKDG perspective, a slope limiter is required to maintain stable numerical solutions [11,33,39]. In this work, two reference RKDG-schemes for shallow water modelling are used, each with its selection of strategies for the aforementioned issues.

Scheme 1 is a scheme based on the well-balancing strategy proposed by [36], relying on a continuous projection of the bed $\underset{\sim}{z}$ into the discrete DG space (specifically, continuous at cell edges), thus eliminating the ill-posed Riemann problem issue that gives rise to non-well-balanced schemes. The bed projection in this work is kept at $p = 1$, regardless of the accuracy of the method, for practical reasons. Therefore its limitation is that, even when computing with $P > 2$, the bed projection remains linear [31,36]. The strategy presented by [36] also guarantees depth-positivity for RKDG2 by enforcing that the solution remains positive at cell edges. Therefore, if the value of depth at the edge is smaller than a prescribed dry-threshold value ϵ_d, the projected depth function $\underset{\sim}{h}$ is modified to guarantee positivity. Following this modification, momentum is modified accordingly, computing it with the depth-positive values, as well as a temporary redefinition of the projected bed, to ensure well-balancing in a partially-wet cell. A relevant observation is that the strategy is not directly extensible to RKDG3, but for the test cases shown in this work, it is not needed. Finally, as for the slope limiter, the strategy suggested in [33] is used, which requires the choice of a shock-detector parameter $\epsilon_{\hat{\delta}}$ [39]. When in presence of friction, the friction term is discretized following [36,42].

Scheme 2 uses the well-balancing strategy proposed by [67], which introduces a correction for the numerical fluxes based on a hydrostatic reconstruction [3]. This strategy has the advantage that it is general as it can handle higher-order beds and solutions, and allows for mathematical discontinuities in the bed projection $\underset{\sim}{z}$. However, it introduces errors when the flow is not hydrostatic because of the nature of the reconstruction [3]. Positivity is ensured by applying a positivity-preserving limiter [70] at partially-wet cells. This limiter, in an RKDG2 context effectively rotates the solution over its mean value to ensure positivity in the entire cell, thus potentially perturbing the well-balanced property. On fully wet cells, a TVD limiter on the characteristic variables is applied [10] for stability.

Finally, for the steady problems presented herein, imposed depth/discharge boundary conditions are treated as first-order accurate (and thus limited to such accuracy), i.e., the solution is assumed to have only $\mathbf{U}_{i,k}0 = \mathbf{U}_{\text{bnd}}$ and all other $\mathbf{U}_{i,k} = 0$, $\forall\, 0 < k \leq p$. This avoids defining slopes at boundaries, which are normally not supplied as physical information at the boundary, since such information is rarely available in real applications. This is a compromise on global accuracy, but favours steady flows to remain steady. Other types of boundaries, e.g., reflective and outflow boundaries, are kept consistent with the order of the RKDG scheme throughout the presented cases.

4. Adaptivity and multiresolution analysis

This work relies on the strategy for solution-based mesh adaptation within the MWRKDG context as proposed by [20]. Its extension to cope with the aforementioned issues relating to the shallow water equations has been formally studied from a mathematical point of view [18]. The presentation of the adaptive strategy in this paper intends to be less formal, but more practical, in the sense that it aims to provide the relevant information to execute the adaptive process, without presenting the underlying formal mathematics. In compliance with the scope of this paper, it is also restricted to

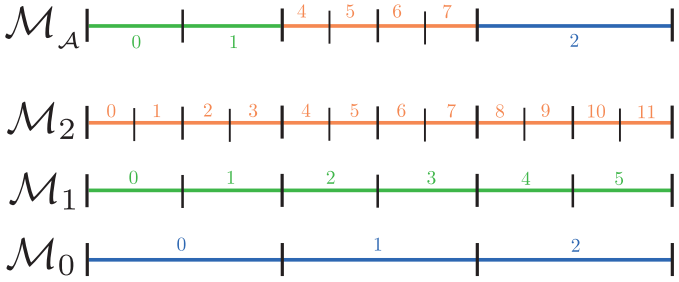

Fig. 1. Nested mesh hierarchy.

one-dimension. The reader is referred to [18,20] for details, proofs and the 2D framework. For further technical description on the 1D SW-MWRKDG adaptive scheme, the reader is referred to [31].

Adaptivity is a process through which an adaptive mesh $\mathcal{M}_{\mathcal{A}}$ is found, a mesh which entails different resolution levels. This mesh should be an optimal non-uniform mesh on which to numerically solve the shallow water equations. Therefore, the whole SW-MWRKDG scheme is actually a process requiring three distinct steps, two of which are for adaptivity itself. They are *prediction* and *hard thresholding*. The prediction phase is concerned with refinement, while the hard thresholding phase is concerned with coarsening. In between them is the third step, in which the actual RKDG evolution of the degrees-of-freedom, i.e., Eq. (13), is performed. The adaptive strategy is based on two key concepts: a hierarchy of nested meshes and multiresolution analysis, by means of multiresolution transformations supported on multiwavelets.

4.1. Mesh hierarchy

The mesh hierarchy $\mathcal{M} = \{\mathcal{M}_0, \mathcal{M}_1, \ldots, \mathcal{M}_L\}$ is a set of $L+1$ nested meshes built by selecting an initial baseline mesh $\mathcal{M}_0$ with $\mathcal{N}_0$ cells, i.e., the coarsest mesh in the mesh hierarchy and L the number of additional resolution levels over the baseline mesh. The successive levels $l \leq L$ are built by dyadically, and recursively, dividing the cells, as shown in Fig. 1. This clearly leads, in one-dimension, to $\mathcal{N}_l = 2^l \mathcal{N}_0$ cells at each level. Fig. 1 also shows an example of an adaptive mesh, combining cells from different levels.

To define the nestedness of cells, and to define the notation used henceforth, consider a cell I in any particular level $l < L$. Then, the refinement set $\mathcal{R}_\mathrm{I}$ is the set of *finer* cells i on level $l+1$ which are contained within cell I, defined as

$$\mathcal{R}_\mathrm{I} = \{2\mathrm{I}, 2\mathrm{I}+1\} \tag{15}$$

The refinement set clearly establishes the two-level relationship between two fine cells i and their coarser cell I. This two-level relation is of course generalizable by recurrence.

4.2. Multiresolution analysis

Multiresolution analysis [45] is the process through which the information contained in the single-resolution (or single-level) solution is decomposed by the multiresolution transformation into *multiple resolution levels*. The information across levels is then evaluated to identify if there are different significant magnitudes of information embedded within the RKDG solution. In this context, the RKDG local polynomial solution can be represented by a coarse resolution dataset, which can be decomposed into higher resolution information, encoded into (detail) coefficients.

To describe the concept, consider Fig. 2 where the solutions at two successive resolution levels are shown, i.e., $\underset{\sim}{\mathbf{U}}_i$ and $\underset{\sim}{\mathbf{U}}_\mathrm{I}$ in subfigure ① and ②, respectively. Clearly, from the RKDG approximation, Eq. (9), the approximate solution in ① can be described by fine resolution coefficients $\mathbf{U}_{i,k}$ and basis functions $\varphi_{i,k}$ as in ④. This is also true for the coarse solution $\underset{\sim}{\mathbf{U}}_\mathrm{I}$ in subfigure ② which can be described by coarse resolution coefficients $\mathbf{U}_{\mathrm{I},k}$ and basis functions $\varphi_{\mathrm{I},k}$ as in ⑤. The difference between the fine solution $\underset{\sim}{\mathbf{U}}_i$ and the coarse solution $\underset{\sim}{\mathbf{U}}_\mathrm{I}$ is encoded as in ③.

Alternatively, another representation can be established via the *two-resolution transformation*. This allows to express the finer solution $\underset{\sim}{\mathbf{U}}_i$ in terms of the coarse solution $\underset{\sim}{\mathbf{U}}_\mathrm{I}$ and some *details* $\mathbf{D}_{i,k}$ related to *multiwavelet* functions $\psi_{i,k}$. $\mathbf{D}_{i,k}$ represents a vector of details associated to each of the conserved variables, i.e., $\mathbf{D}_{i,k} = [d_h, d_q]^T_{i,k}$. The multiwavelets span a set of spaces $\mathbf{W}_l = \mathrm{span}\{\psi_{i,k}\}$. Importantly, as shown in Fig. 2, $\psi_{i,k} \in \mathbf{W}_l$ (and not $\psi_{i,k} \in \mathbf{W}_{l+1}$, which could easily be mistaken for). The solution subspaces $\mathbf{V}_l = \mathrm{span}\{\varphi_{i,k}\}$ and the wavelet subspaces $\mathbf{W}_l$ are orthogonal complements and satisfy $\mathbf{V}_{l+1} = \mathbf{V}_l \oplus \mathbf{W}_l$. The wavelets are orthonormal in L^2, have compact support (have non-zero values within the cell only) and have a number of vanishing moments $\overline{M} \leq p$ [20].

The two-resolution transformation can be used to *decode* (following the traditional signal-processing terminology) or *promote* (term preferred herein) a local solution from a lower level into a higher level, that is, conceptually ② + ③ → ① or equivalently ⑤ + ⑥ → ④. Alternatively, the transformation may be used to *encode* (signal-processing term) or *demote* (term preferred herein) a local solution

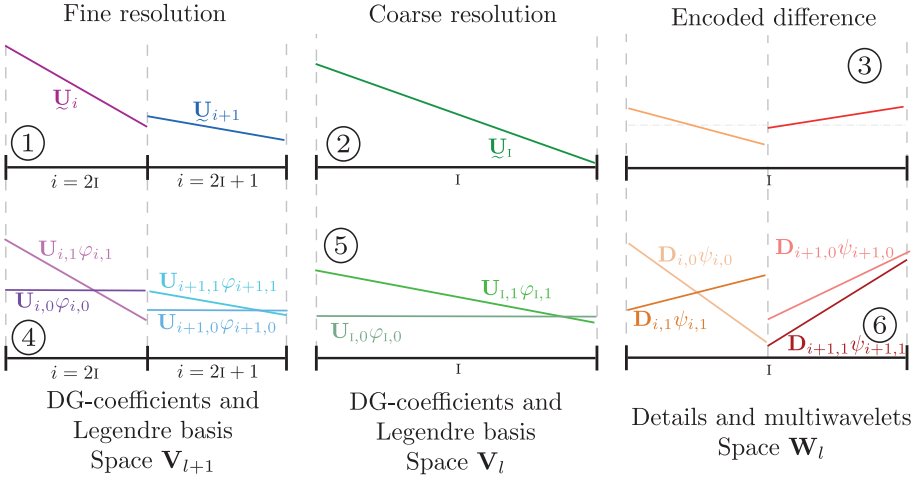

Fig. 2. Piecewise polynomial solution projection (top) and its decomposition into modal (bottom) representation. Multiresolution decomposition is shown as an encoded difference linking information across cells I and i.

from a higher level into a lower level, that is

$$① \rightarrow \begin{cases} ⑤ \rightarrow ② \\ ⑥ \rightarrow \text{stored} \end{cases} \tag{16}$$

Note that, when demoting, the coarser details shown in ⑥ are not really necessary to rebuild the coarse solution in ②. It suffices to know the coefficients shown in ⑤.

Formally, and mathematically, the two-resolution transformation is

$$\underbrace{\underline{\mathbf{U}}_i}_{①} = \underbrace{\sum_{k=0}^{p} \mathbf{U}_{i,k}\,\varphi_{i,k}}_{④} = \underbrace{\sum_{k=0}^{p} \mathbf{U}_{1,k}\,\varphi_{1,k}}_{\underline{\mathbf{U}}_1,\ ⑤} + \underbrace{\sum_{i=2\imath}^{2\imath+1}\sum_{k=0}^{p} \mathbf{D}_{i,k}\,\psi_{i,k}}_{⑥} \tag{17}$$

Because the multiwavelets are an orthonormal set of basis functions, the detail coefficients $\mathbf{D}_{i,k}$ are found to be

$$\mathbf{D}_{i,k} = \int \underline{\mathbf{U}}_1 \psi_{i,k}\,dx \tag{18}$$

However, for practical reasons and for efficiency, the multiresolution transformation is not applied directly, since what is of interest is to demote (encode) or promote (decode) the coefficients, and not the solution itself. The demotion (encoding) transformations can be expressed as

$$\mathbf{U}_{1,k} = \sum_{i=2\imath}^{2\imath+1}\sum_{j=0}^{p} \mathbf{U}_{i,j} \int \varphi_{i,j}\varphi_{1,k}\,dx \tag{19}$$

$$\mathbf{D}_{1,k} = \sum_{i=2\imath}^{2\imath+1}\sum_{s=2\imath}^{2\imath+1}\sum_{j=0}^{p} \mathbf{U}_{i,j} \int \varphi_{i,j}\psi_{s,k}\,dx \tag{20}$$

The promotion (decoding) transformation is

$$\mathbf{U}_{i,k} = \sum_{j=0}^{p} \mathbf{U}_{1,k} \int \varphi_{1,j}\varphi_{i,k}\,dx + \sum_{j=0}^{p} \mathbf{D}_{1,j} \int \psi_{1,j}\varphi_{i,k}\,dx \tag{21}$$

These transformations have the very appealing and convenient property that they allow to promote or demote the solution across resolution levels using decomposed information of the solution itself, without the need for any artefacts to reconstruct the solution. This allows to conserve the accuracy of the solution when cycling over the transformations.

4.3. Adaptivity

4.3.1. Filtering criteria: significant details

One of the most relevant issues when performing adaptivity, is to establish a robust criterion that identifies which regions have a solution that require higher spatial resolution because of its spatial variability. In the SW-MWRKDG strategy this criterion is based on the concept of *significant details* $\breve{d}_{i,k,c}$, where c is an index which spans the components of the conserved variables vector $\mathbf{U}$. Significant details are identified by

$$\breve{d}_{i,k,c} = \begin{cases} d_{i,k,c}, & \text{if } \max\limits_{c\in[h,hu]} \left(\dfrac{|d_{i,k,c}|}{\max\left[\max\limits_i(\mathbf{U}_{i,0,c}), \sqrt{\delta x_i}\right]} \right) > \epsilon_l \\ 0, & \text{otherwise} \end{cases} \tag{22}$$

where ϵ_l is a level-dependent threshold value defined as

$$\epsilon_l = \epsilon_a 2^{l-L} \tag{23}$$

where ϵ_a is the user-prescribed threshold value for adaptivity. This is the *only* value that must be specified by the user to control the adaptive process. The choice of this threshold value follows the guidelines recommended in [19,20]. For realistic problems, the choice of the threshold value responds to the accuracy at which the smallest flow feature of interest needs to be modelled. These features might be, for example, travelling waves or wet-dry fronts.

Eq. (22) allows to assess if any component of the details vector (associated to a conserved variable, for every polynomial coefficient) is significant relative to all others in the same level. Therefore, details are normalised within the context of the entire problem, including different physical quantities and levels of accuracy. Note that the normalisation process is performed component-wise, spanning the conserved variables. That is, when the fraction is evaluated, a dimensionless quantity is obtained relative to each conserved variable, and then the maximum value among such dimensionless quantities is chosen.

Very importantly, the conserved variables vector during the adaptive process must be recasted as $\mathbf{U} = [h+z, q]^\top$, so that it is not depth, but water surface elevation, that is analysed by the multiresolution transformations. This acknowledges that, in presence of a non-constant bed, depth is a poor indicator of regularity/complexity of the solution, e.g., constant depth does not necessarily mean a quiescent flow, which would erroneously lead to non-significant details under uniform flow conditions. Furthermore, such recasting ensures that the well-balancing property of the scheme is transparently carried into the adaptive scheme [18].

In an analogous way to the details $d_{i,k,c}$ of the solution, it is necessary to define details $b_{i,k}$ associated to the topography. Note that the bed details are a set of scalars only, not a set of vectors as the conserved variables, therefore the c subindex is superfluous. All the previously defined transformations are analogous, but instead of demoting or promoting the solution coefficients $\mathbf{U}_{i,k}$, bed details allow to transform the bed (DG-projected) coefficients $z_{i,k}$. Alternatively, it would be possible to include $z_{i,k}$ within an extended version of the details $d_{i,k,c}$, but such approach is inconvenient, since the bed does not evolve in time and therefore there is no need to adapt the mesh to the bed at every time step. In particular, since the optimal mesh to represent topography can be determined at the beginning, any additional refinement should only respond to the flow (evolution of conserved variables). On the other hand, no coarsening should happen, since it would reduce the accuracy of the bed representation. By keeping $b_{i,k}$ separate from the details $d_{i,k,c}$, it is possible to ensure that the aforementioned coarsening effect is avoided, thus preserving bed accuracy. The practical effect of this is that the adaptive mesh is not allowed to generate cells which are coarser than those required by the topography at a particular position, even if the flow conditions (details of the conserved variables) allow for coarser cells there. The significant bed details $\breve{b}_{i,k}$ are determined analogously to the significant flow details $\breve{d}_{i,k,c}$, following

$$\breve{b}_{i,k} = \begin{cases} b_{i,k}, & \text{if } \dfrac{|b_{i,k}|}{\max\left[\max\limits_i(z_{i,k}), \sqrt{\delta x_i}\right]} > \epsilon_l \\ 0, & \text{otherwise} \end{cases} \tag{24}$$

4.3.2. Prediction

Prediction is the process through which, based on the available information at the current time, the mesh is adapted to accommodate for a more accurate update into the next time. To perform prediction, Eq. (22) is used to find which details are relevant at a level, progressively from low to high. As details in finer levels are analysed they may stop being significant. Those levels at which details are significant need to be kept in the adaptive mesh, and therefore cells are promoted (refined) up the highest level which contains significant details. Higher levels with non-significant levels are therefore not necessary. Refinement, in this context specifically means to promote a coarse cell $\imath$ (in level l one level up, into two cells $i = 2\imath$ and $i = 2\imath + 1$ (in level $l+1$), if $|\breve{d}_{i,k,c}| > 0$, notably, with details referring to level l. This constitutes the cornerstone of the prediction process. Additional criteria is enforced during prediction for several purposes:

1. To keep topography discretization at its required level, refinement is enforced at a cell i if $|\breve{b}_{i,k}| > 0$, regardless of $\breve{d}_{i,k,c}$.
2. To ensure that significant details can accurately move into neighbouring cells, refinement is triggered at cells which are neighbour of a cell with significant details $|\breve{d}_{i,k,c}| > 0$.
3. To ensure that steep gradients, which may evolve into shocks are accurately captured during update, refinement is triggered at cells i with $|\breve{d}_{i,k,c}| > 2^{\overline{M}+1}\epsilon_l$.

This process results in a *predicted* mesh denoted by $\mathcal{M}^{\star}_{\mathcal{A}}$.

4.3.3. Multiresolution update

After the prediction step, the RKDG evolution is performed for a single time step following Eq. (13), over each cell of the adaptive mesh (which of course may include different resolution levels). This only requires performing the same process as a non-adaptive RKDG computation, because of its inherent locality. In order to do so, the solution is reconstructed within the cells of the predicted adaptive mesh $i \in \mathcal{M}_{\mathcal{A}}$, numerical fluxes are computed on the edges of the adapted cells and quadrature rules are performed, finally obtaining the updated polynomial coefficients of the RKDG solution.

4.3.4. Hard thresholding

The hard thresholding process is performed after updating in order to coarsen regions which are no longer necessary to keep at high resolution. It can be simply expressed as filtering negligible detail coefficients by strictly zeroing (thus, *hard* thresholding) coefficients evaluated as non-significant. That is, a cell i can be coarsened one level if all of its $\breve{d}_{i,k,c} = 0$ and $\breve{b}_{i,k} = 0$, following Eqs. (22) and (24).

4.3.5. Full adaptive solution algorithm

Algorithm 1 summarises the entire adaptive solution process.

Algorithm 1 SW-MWRKDG

1: Initial projection of the solution and the bed, following Eq. (10) with $\varphi_{i[L],k}$, at the highest resolution level.
2: Initial thresholding of bed and solution to obtain initialadaptive mesh $\mathcal{M}^n_{\mathcal{A}}$.
3: **for all** Time steps in simulation **do**
4: **procedure** PREDICTION
5: Determine coefficients from the solution in $\mathcal{M}^n_{\mathcal{A}}$ through the demotion multiresolution transformation, Eqs. (19) and (20)
6: Find and flag significant details, Eq. (22)
7: Determine the predicted adaptive mesh $\mathcal{M}^{\star}_{\mathcal{A}}$ by assessing significant details, and reconstruct the solution in $\mathcal{M}^{\star}_{\mathcal{A}}$ through the promotion transformation, Eq. (21).
8: Perform positivity correction of higher-order coefficients
9: **end procedure**
10: **procedure** UPDATE
11: **for all** Runge-Kutta stages **do**
12: Impose boundary conditions
13: RKDG update on the $\mathcal{M}^{\star}_{\mathcal{A}}$ mesh, Eq. (13)
14: At the highest level cells only, perform limiting and ensure depth-positivity
15: **end for**
16: **end procedure**
17: **procedure** HARD THRESHOLDING
18: Determine coefficients from the solution in $\mathcal{M}^{\star}_{\mathcal{A}}$ through the demotion multiresolution transformation, Eqs. (19) and (20)
19: Find and flag significant details, Eq. (22)
20: Determine the thresholded adaptive mesh $\mathcal{M}^{n+1}_{\mathcal{A}}$ by assessing significant details
21: Perform positivity correction of higher-order coefficients
22: **end procedure**
23: Set $\mathcal{M}^{n+1}_{\mathcal{A}} = \mathcal{M}^n_{\mathcal{A}}$, and $\mathbf{U}^n_{i,k} = \mathbf{U}^{n+1}_{i,k}$.
24: **end for**

5. Numerical tests

This section presents four well-known benchmark test cases for 1D shallow water problems with source terms. The first test addresses quiescent flow over non-differentiable topography. The second is concerned with steady flow with transcritical shock over a frictional, complex topography. The third addresses moving wet-dry fronts in a parabolic basin, and the fourth is an experimental dam break problem over a frictional bed with an obstacle.

The numerical tests reported herein seek to (i) study how do two different numerical schemes perform in an adaptive context and the impact of adaptivity on the features of such schemes, (ii) show how the adopted strategy preserves the quality of the solution, when compared to the uniform-mesh solution, (iii) show the advantages of the adaptive scheme in particular with features of real shallow flows, such as complex beds, shocks, wet-dry fronts and friction (iii) establish the potential advantages and shortcomings of the SW-MWRKDG strategy with regards to real shallow flows and flood modelling.

Results in this section were computed using the two RKDG2 schemes described in Section 3.1, i.e., $P = 2$, unless mentioned otherwise. The baseline mesh $\mathcal{M}_0$ for all cases has $\mathcal{N}_0 = 2$ cells, and adaptive computations were preformed with $L = 8$ levels, which results in $\mathcal{N}_L = 512$ cells. Some non-adaptive computations were performed with different number of cells, and are presented when necessary. The dry threshold was fixed to $\epsilon_d = 0.001$ which has been deemed enough for RKDG2, and for comparison purposes the adaptive threshold was set to $\epsilon_a = 0.1$ unless stated otherwise.

5.1. Flow over non-differentiable topography

This case features a non-differentiable topography, defined by a set of piecewise constant elevations. It has been previously used to test for well-balancing of shallow water schemes [14,36]. In this work, the case is used to study how the two chosen reference schemes interact with the adaptive strategy in terms of well-balancing. Two subcases are presented. The first subcase features a fully wet domain with quiescent conditions. The second subcase also features a quiescent state, but with two wet-dry fronts.

Results are presented for both reference schemes, for both non-adaptive (uniform) and adaptive simulations. Non-adaptive results were computed with a fine mesh named L8 ($\mathcal{N}_L = 512$) and a coarse mesh named L4 ($\mathcal{N}_L = 32$). Adaptive results were computed for an adaptive hierarchy with $L = 8$. Results are shown for $t = 100$ s. If a longer time were selected, numerical perturbations of the initially quiescent state would be dampened by the end of the simulation. For this reason, the simulation time is kept at $t = 100\,s$ to properly evaluate the schemes' ability to keep the C-property.

For both quiescent cases, boundary conditions were set to be reflective, and initial conditions were $q = 0$ and $h + z = 12$ m for the fully wet case, and $h + z = 6.5$ m for the partially wet case.

5.1.1. Fully wet quiescent flow

Fig. 3 shows the results for the fully wet quiescent case. As Figs. 3(a) and (b) show, both reference schemes when performing uniform-mesh simulations, are able to keep the quiescent state perfectly, with zero discharge (up to machine precision), for both the fine (L8) and coarse (L4) meshes. Note how the bed is projected differently by both reference schemes, which is particularly clear for the coarse L4 mesh. Figs. 3(c) and (d) show that adaptive simulations also keep the quiescent state accurately, although with some introduction of numerical error (with an order of magnitude of up to 5×10^{-9}). Figs. 3(c) and (d) also show the refinement pattern, which is clearly

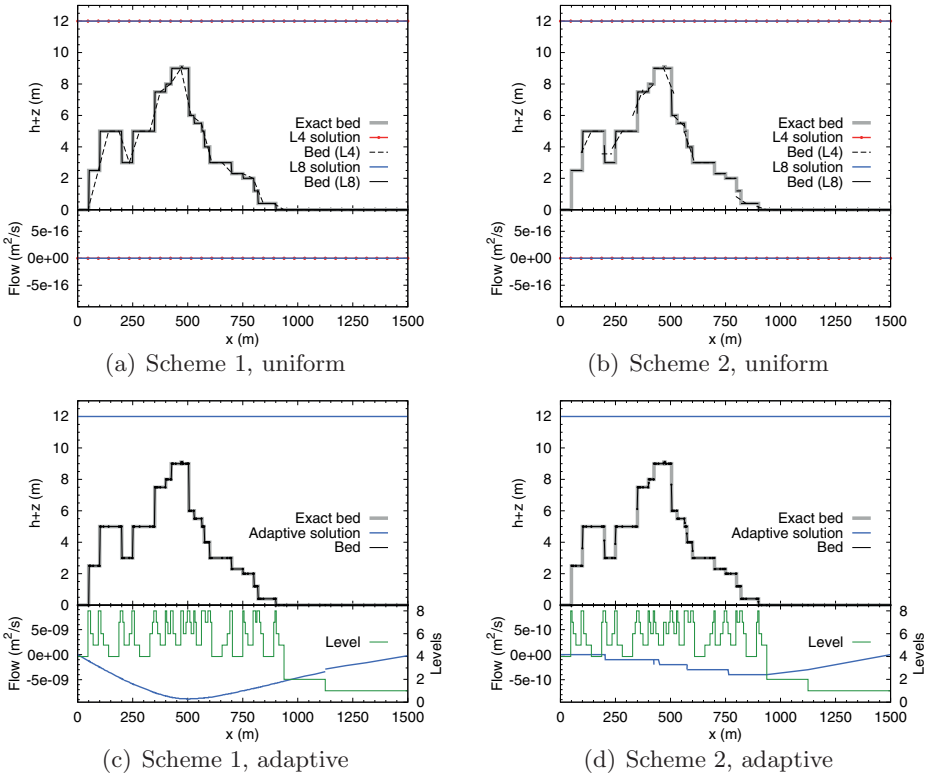

(a) Scheme 1, uniform (b) Scheme 2, uniform

(c) Scheme 1, adaptive (d) Scheme 2, adaptive

Fig. 3. Uniform and adaptive results with two reference schemes for fully wet quiescent flow over a non-differentiable topography.

driven only by topography. Because the exact bed features discontinuities, the adaptive scheme refines to the highest level at such locations. The adaptive pattern obtained with the two different reference schemes are very similar, and the resulting number of cells are 108 (Scheme 1) and 106 (Scheme 2) cells.

It is not surprising that both schemes achieve a good quiescent solution. Scheme 1, because it enforces bed continuity simply eliminates the ill-posedness of the Riemann problem at cell interfaces. The trade-off can be, as shown by the L4 non-adaptive result, that discontinuous topography can be smeared. On the other hand, scheme 2 is designed from a hydrostatic state assumption, and corrects the flux term to ensure that hydrostatic equilibrium is guaranteed. It is therefore designed to do specifically this, to keep a quiescent state.

5.1.2. Quiescent flow with wet-dry regions

Fig. 4 shows the results for the partially wet quiescent case. Fig. 4(a) shows that reference scheme 1 is able to perfectly keep the quiescent state for both the coarse and fine meshes. The coarse (L4) solution clearly shows that the scheme can handle partially wet cells (as shown by the partially wet cell at $x \approx 350$ m). Scheme 1 involves a correction of RKDG coefficients so that, in the event of a partially wet cell, no momentum is generated when reshaping the (cell) local water surface function to ensure positivity. Notably, mesh resolution does not affect the preservation of the quiescent state with Scheme 1. Fig. 4(b) shows that reference scheme 2 is unable to keep the quiescent state. The wet-dry strategy in Scheme 2 reshapes the water surface to enforce depth-positivity, and by doing so creates momentum when the cell is (initially) partially wet. The perturbed state is clear both in terms of water surface and discharge for L4, but only clear for discharge in L8. From Fig. 4(b) it can also be extracted that coarse solutions (L4) are likely to be poorly well-balanced (larger perturbations of a quiescent state, in this particular case) than finer solutions (L8). This is expected, since the momentum wave created depends on how much the solution needs to be reshaped which in turn responds to cell size. Therefore, mesh refinement can alleviate this issue for Scheme 2.

Adaptive results for Scheme 1 are shown in Fig. 4(c). The figure shows that the quiescent state is preserved accurately. Discharge shows deviations from zero in the magnitude of 10^{-10}, which are introduced by truncation errors in the arithmetic of the adaptive process, and are acceptable. Fig. 4(d) shows adaptive results for Scheme 2. The water surface profile in this figure looks deceivingly correct, i.e., it looks constant and perfectly quiescent. However, the discharge is highly perturbed, with variations in the order of 0.3 m^2/s, which are definitively not acceptable for a quiescent state. Interestingly, the adaptive scheme can again alleviate, but cannot solve, the non well-balancedness of Scheme 2 for partially wet cells, in the sense that the water surface profile is improved (when compared with the uniform L4), following the previous discussion on resolution for Scheme 2.

CPU time for both the wet-wet and wet-dry quiescent cases is shown in Table 1. The table shows that all adaptive cases provided a speed up, on average around 2.5 when compared to the uniform L8 case. On the other hand, clearly, coarse meshes are significantly cheaper in terms of computational time. Notice that adaptive results show cells mostly between levels 4 and 8, and that CPU time is, clearly not reduced to the levels of L4, but significantly nonetheless. Finally, it is clear that the modest speed-up comes from the proportionally

Table 1
CPU time for quiescent cases.

Case	Scheme	CPU time (*s*)			Speed-up
		Uniform L4	Uniform L8	Adaptive L8	
Wet-Wet	1	0.02	4.81	1.48	3.25
	2	0.01	1.63	0.64	2.54
Wet-Dry	1	0.01	1.10	0.69	1.59
	2	0.01	1.16	0.44	2.63

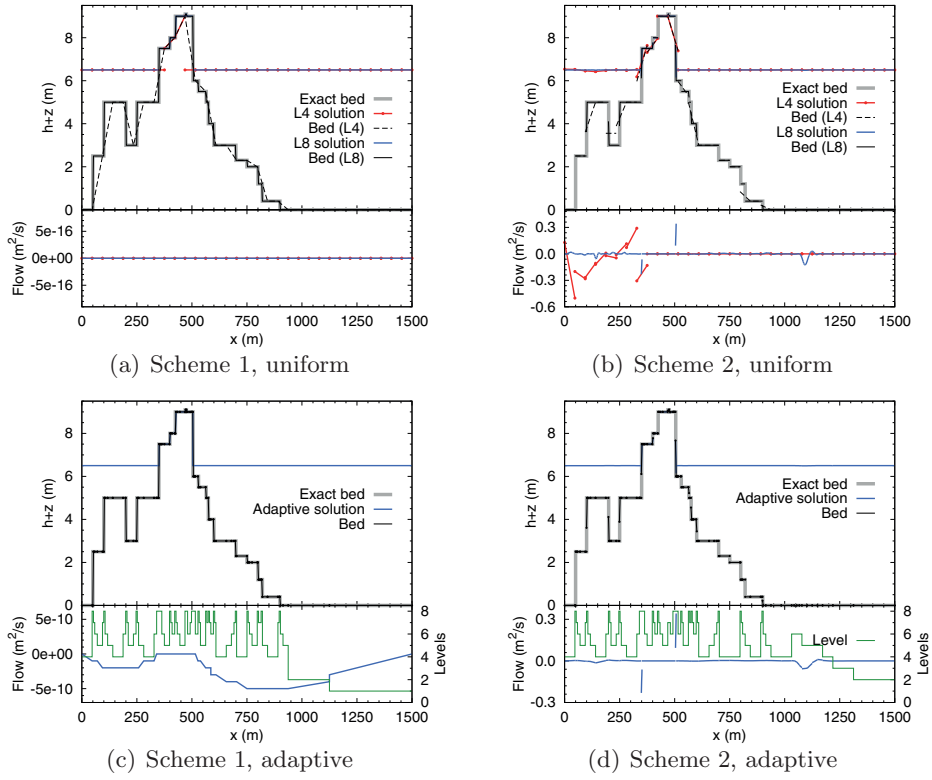

(a) Scheme 1, uniform (b) Scheme 2, uniform

(c) Scheme 1, adaptive (d) Scheme 2, adaptive

Fig. 4. Uniform and adaptive results with two reference schemes for partially-wet quiescent flow over a non-differentiable topography.

large number of high resolution cells required to represent a discontinuous topography.

5.2. Transcritical steady flow with shock

This test case is based on the setup proposed by [44] as *'Problem 6'*. It features 1D steady flow with friction over a changing bed, with two transcritical points, one of which is a shock. This case has been chosen to show that the adaptive scheme can properly handle all the real features of a flow, and indeed converge over a transient to a steady solution. Furthermore, since steady flow is achieved, comparisons with different meshes and RKDG-accuracy can be performed easily.

The case consists of a rectangular prismatic channel of width $B = 10\,\text{m}$, length $L = 200\,\text{m}$, and a steady flow of $Q = 20\,\text{ms}^{-3}$. Since the present shallow water model follows a unit-width formulation, boundary conditions are as follows: an inflow of $q = Q/B = 2\,\text{ms}^{-2}$ is imposed in the upstream boundary and depth $h = 1.700225\,\text{m}$ is imposed at the downstream boundary. The initial condition was set as a constant water elevation $h + z = 4\,\text{m}$.

The analytical steady state solution for $x < 100$ is

$$\hat{h}(x) = 0.741617 - \frac{0.25}{\tanh(3)} \tanh\left(\frac{3}{50}(x - 50)\right) \tag{25}$$

For $x > 100$ the solution is

$$\hat{h}(x) = e^{-p(x-x^\star)} \sum_{i=0}^{M} k_i \left(\frac{x - x^\star}{x^{\star\star} - x^\star}\right)^i + \phi(x) \tag{26}$$

with

$$\phi(x) = \phi_b \exp \phi_c (x - \phi_d) \tag{27}$$

and $x^\star = 100$, $x^{\star\star} = 200$, $M = 4$, $p = 0.3$, $k_0 = 1.0656$, $k_1 = 0.0604859$, $k_2 = -0.00423834$, $k_3 = 0.00198394$, $k_4 = -0.00144967$, $\phi_b = 1.7$, $\phi_c = 0.005$ and $\phi_d = 200$. This solution defines a subcritical region for $x < 50$, a supercritical region for $50 < x < 100$ and a subcritical region for $x > 100$.

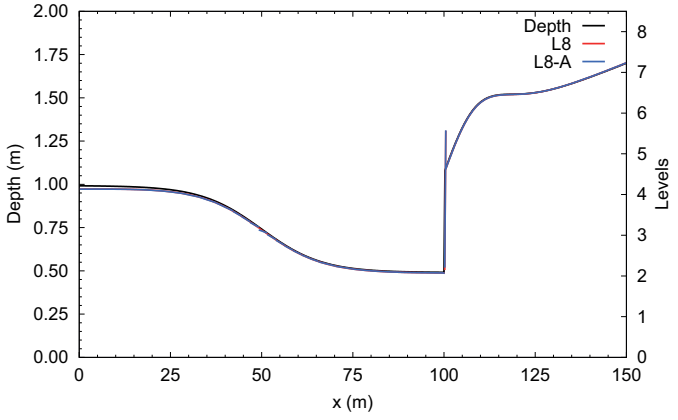

Fig. 5. Adaptive and uniform depth results when steady flow has been achieved for MacDonald test case.

Bed slope is given by

$$\frac{\partial z}{\partial x} = \left(1 - \frac{Q^2 B}{g\hat{h}^3(x) B^3}\right) \frac{\partial \hat{h}}{\partial x} + \frac{Q^2 n^2 \left(B + 2\hat{h}(x)\right)^{4/3}}{\hat{h}^{10/3}(x) B^{10/3}} \tag{28}$$

The case was run with Manning's coefficient set to $n = 0.02$. The simulation was computed for $1000\,s$, a time for which steady flow is already reached.

Figs. 5 through 8 show results for both adaptive and uniform computations with Scheme 1, together with the exact solution. The full solution $\underset{\sim}{\mathbf{U}}$ is shown with solid lines, while mean values $\mathbf{U}_{i,0}$ are shown with markers. In general terms, the numerical steady state solutions match the analytical solution well. Small differences exist and are due to the chosen discretization of the friction source term, here discretized following [36,42], which in turn is a generalisation of FV techniques [5,8,17,49,59]. This friction modelling technique

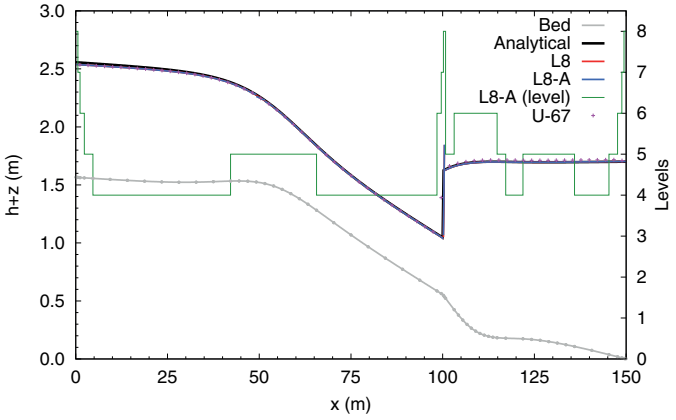

Fig. 6. Water surface and adaptive refinement level at steady flow for MacDonald test case.

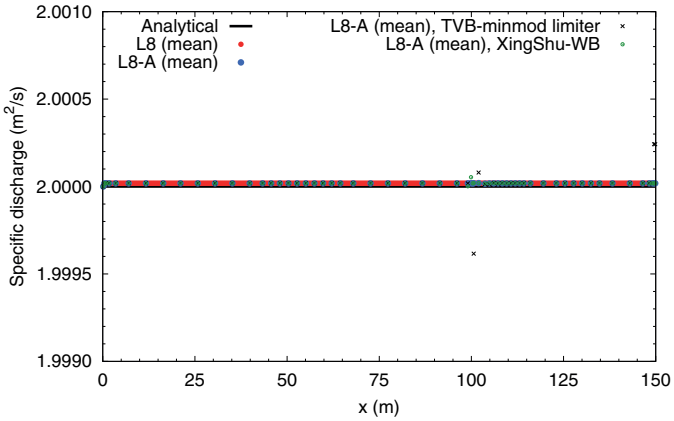

Fig. 7. Steady state discharge, uniform and adaptive results for MacDonald test case.

is commonplace, but has nevertheless been shown to result in somewhat inaccurate solutions clearly observable in steady cases [8,48], since it does not properly balance the equation. Uniform (L8) and adaptive (L8-A) solutions overlap almost fully. This illustrates that the adaptive strategy does not reduce accuracy when compared to the equivalent uniform high resolution mesh, fully consistent with previous results [18,31].

Fig. 6 also clearly shows the resolution levels throughout the domain under steady flow. Note that the minimum resolution is predicted at level 4, and the maximum at level 8. Maximum resolution is only obtained at the shock ($x = 100$ m) and at both boundaries. Boundaries are kept at the highest resolution to avoid possible perturbations of the steady state discharge. Intermediate levels of resolution are obtained at $x = 50$ m where the flow transitions from subcritical to supercritical, and therefore relevant waves are propagating. The adaptivity clearly also responds to the bed at $100 \leq x \leq 140$ where the bed slope changes, thus requiring levels 5 and 6 of resolution.

The adaptive solution results in 67 cells when steady flow is achieved. This represents only 13% of the highest resolution uniform mesh. Clearly, a significant gain is achieved in terms of computational cost, while preserving high spatial resolution at those regions where it is necessary and convenient. To further illustrate the gain in quality by using the adaptive strategy, additional results were computed with a uniform mesh of 67 cells (U67), and also shown in Fig. 6 for comparison. Only the mean values are shown for clarity in the figure. Note how the U67 solution fails to capture the shock as accurately as L8-A or L8. Furthermore, the subcritical region $x > 100$ is slightly less accurate as well. These differences show that the adaptive scheme can optimally use cells to minimise errors at the same computational cost.

Fig. 7 shows the results for specific discharge (momentum). Note that both the uniform and adaptive solutions capture the steady discharge throughout the domain. In particular, the mean values (zero-order coefficients) of both the uniform (not shown, for clarity) and adaptive solutions are accurate. Around the shock, the limiting strategy chosen for the reference scheme allows the slope of the numerical solutions to be very high, but ensures that the mean values – responsible for conservation– remain accurate [33]. Furthermore, as can be seen in the figure, this feature of the reference numerical scheme is preserved by the adaptive scheme (both non-adaptive and adaptive solutions have this feature). For comparison, computations with an alternative limiting strategy [10] termed here TVB-minmod (used in [18]) were also performed, which resulted in small perturbations of the mean value of the momentum around the shock. Additionally, for comparison, computations with Scheme 2 were performed. The results also show a small perturbation of the mean values. These comparisons show that, depending on the choice of strategies of the *reference* (non-adaptive) RKDG scheme, results can vary, specially for discharge. The adaptive strategy, on the other hand, transparently uses the information from the reference RKDG scheme, and because of the increase in local resolution, can keep the error to a minimum.

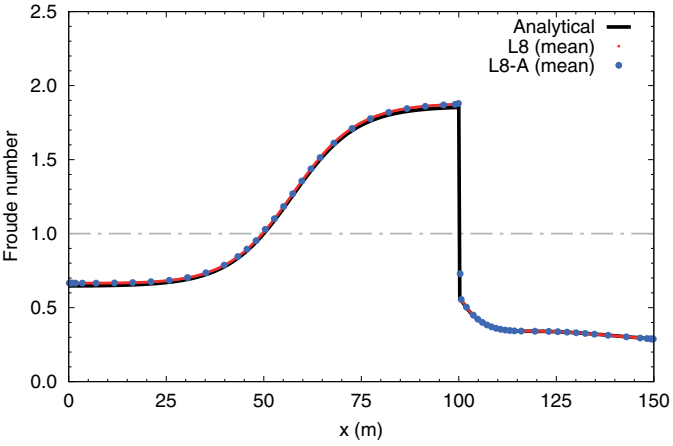

Fig. 8. Froude number (mean value) results at steady state uniform and adaptive results of the MacDonald test case.

Fig. 8 shows the Froude number results. In this figure it is easy to see the features of the solution that may be difficult to appreciate in Fig. 6 because of scale. Notably, critical points and regime changes are well captured by both the uniform and adaptive scheme. Furthermore, since only mean values are represented, it is possible to clearly see how the mesh is adapted around both transcritical points $x = 50$ m and $x = 100$ m and boundaries.

To further show the implications and possibilities of the proposed SW-MWRKDG strategy additional cases were computed. The same test case was computed using SW-MWRKDG3 and the same aforementioned parameters. Adaptive results are shown in Fig. 9 together with the adaptive results with SW-MWRKDG2. The adaptive SW-MWRKDG3 simulation results in 46 cells under steady flow conditions. This is only 9% of $\mathcal{N}_L$, and a 35% increase in the efficiency (in terms of cell number) from $P = 2$ to $P = 3$. In terms of degrees of freedom (DOF), under steady conditions both solutions are almost equivalent, with 134 DOFs for $P = 2$ and 138 for $P = 3$. In Fig. 9, the resolution levels for both $P = 2$ and $P = 3$ are also shown. Note that, at the boundaries and at the shock, both solutions achieve the highest level and the same adaptivity pattern. The reason for this is that boundaries have been set to a fixed resolution level, and that the shock shows the maximum values for detail coefficients in both cases. The differences in the adaptive pattern arise in the smooth regions of the solution, even at the transcritical point at $x = 50$ m.

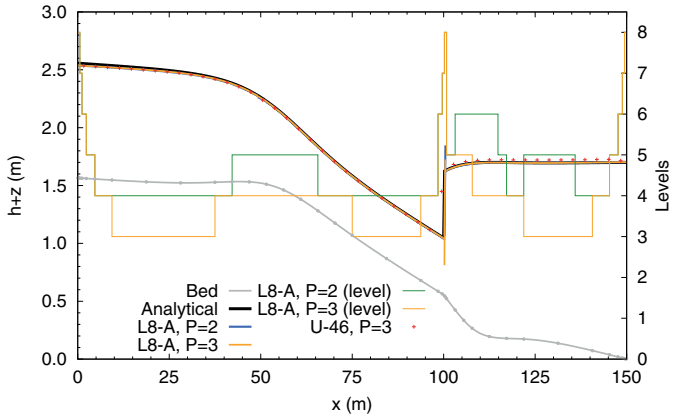

Fig. 9. Comparison of water surface and adaptive refinement level for $P = 2$ and $P = 3$ results for the MacDonald test case.

The $P = 3$ solution systematically requires less resolution than the $P = 2$ in smooth regions while providing a practically indistinguishable steady water surface profile. That is, higher-order solutions can accommodate coarser resolution, and potentially, can efficiently operate with coarse baseline meshes. Finally, a $P = 3$ solution was computed with a uniform mesh of 46 cells. The results also shown in Fig. 9 confirm the previous result for $P = 2$ and 67 cells, namely that, when using the same number of cells, better results are obtained with the adaptive scheme. Note that the solution is relatively inaccurate at the shock, and also in the subcritical region downstream of the shock. This again shows the advantages of adaptivity, which for the same number of cells achieves a better solution.

One last relevant conclusion that may be drawn from this analysis. Recall that the adaptive pattern with SW-MWRKDG3 does not differ from the pattern obtained with SW-MWRKDG2 at shocks but only in smooth region. This suggests that SW-MWRKDG3 could be used in those smooth regions that allow for coarser cells, and SW-MWRKDG2 should be used in those regions near the shock where cells are equally refined for both schemes. This would result in a reduction of computational cost, since SW-MWRKDG2 is cheaper –in terms of operations– per cell than SW-MWRKDG3. In other words, these results clearly suggest to explore polynomial degree adaptivity (p-adaptivity) together with mesh adaptivity within the same multiresolution context, and feeding both adaptive processes with the multiresolution decomposition. This approach would result not only in a reduction in the number of cells, but also in an effective reduction in the number of degrees of freedom.

Finally, CPU time for the uniform L8 case with $P = 2$ was 306.9 s, and for the adaptive 32.4 s (of which around 9 s where required for adaptation processes). That is, the adaptive computation provides a speed-up of 9.5.

5.3. 1D Oscillatory flow in a parabolic bowl

[65] proposed an oscillatory flow in a parabolic bowl and its analytical solution. This case has been extensively used for benchmarking hydraulic models [36,42,70]. It is a rigorous test including a complex bed with a changing slope and moving wetting and drying fronts, and has no interference from boundaries. The goal of performing this test is to study the effects of adaptivity on capturing moving wet-dry fronts. Although an analytical solution with friction exists for this case [58], only the frictionless case is computed here. The reason for this is that the frictionless case is more demanding on the numerical scheme since friction dampens and smooths the solution. Following the results in the previous tests, only Scheme 1 is used in this case.

The bed is described by

$$z(x) = H_0\left(\frac{x}{a}\right)^2 \tag{29}$$

where H_0 and a are constants.

The transient analytical solution for the free water surface is given by

$$\eta(x,t) = H_0 - \frac{B^2}{4g}\cos(2st) - \frac{B^2}{4g} - \frac{x}{g}Bs\cos(st) \tag{30}$$

and momentum is

$$q(x,t) = B\sin(2st)\left[\eta(x,y) - z(x)\right] \tag{31}$$

where s is the frequency

$$s = \frac{1}{2a}\sqrt{8gH_0} \tag{32}$$

The position of the wet-dry front follows

$$x_{wd}(t) = -\frac{Bsa^2}{2gH_0}\cos(st) \pm a \tag{33}$$

Numerical results shown here were computed with $a = 3000$, $B = 5$, and $H_0 = 10$. Under these conditions $T = 1345.94$ s. The simulation was run for until $t = 5000$ s, therefore more than 3.5 periods were computed. Two solutions were computed. A uniform, non-adaptive case with $L = 3$ named L3 consisting of $\mathcal{N}_L = 16$ cells ($\delta x = 625$ m), and L8-A, an adaptive solution with $L = 8$, which implies $\mathcal{N}_L = 512$, with means a maximum resolution of $\delta x_L = 19.53$ m.

Fig. 10 shows the position of the water surface for several times, including the exact solution and both numerical solutions. Note that the L3 solution tracks quite well the exact solution, although, because of the coarse resolution, fails to provide an accurate trail of the wet-dry front. The L8-A results also reproduce the solution accurately, but with the added value of better tracking the wet/dry front. Importantly, note that level 8 is only achieved around the wet/dry front, and that most of the domain is actually in level 3. Furthermore, Fig. 10 clearly shows how the finest cells track the wet-dry front as the transient flow evolves with time.

Since Fig. 10 does not allow to rigorously compare the quality of the solution because of scale, consider Fig. 11, which shows the evolution of maximum water surface error in the domain, i.e., the infinity norm –Eq. (35)– of the error ε defined by Eq. (34). For comparison, several other uniform (non-adaptive) meshes are included and named L4 ($L = 4$, $\mathcal{N}_L = 32$), L6 ($L = 6$, $\mathcal{N}_L = 128$) and L8 ($L = 8$, $\mathcal{N}_L = 512$). Fig. 11 shows that L8-A produces a maximum error which is somewhere in between L4 and L6, and that there is little difference between L6 and L8. But most importantly, there is a large reduction of maximum error when moving from L3 to L8-A, although most of the domain is represented at level 3.

$$\varepsilon_i = \sum\left[\underset{\sim}{\mathbf{U}}(x_i) - \mathbf{U}(x_i)\right]\delta x_i \tag{34}$$

$$L_\infty = \max_{i\in\mathcal{M}_A}(|\varepsilon_i|) \tag{35}$$

Root Mean Square Error (RMSE), as shown in Eq. (36), can also be of interest. RMSE of water surface elevation is shown in Fig. 12. RMSE behaves quite differently than the maximum error. Firstly, note that the L8 results tend to slowly grow in time, showing that the error is being accumulated. The RMSE for L8-A is highly oscillatory in time. It shows values smaller than other cases but can also reach values as high as those obtained from L3. This is reasonable, since a large portion of the domain is on level 3, but the wet-dry front (which is one of the main sources of error, and typically where the maximum local error is at) is computed on level 8.

$$\text{RMSE} = \sqrt{\sum_{i\in\mathcal{M}_A}\varepsilon_i^2} \tag{36}$$

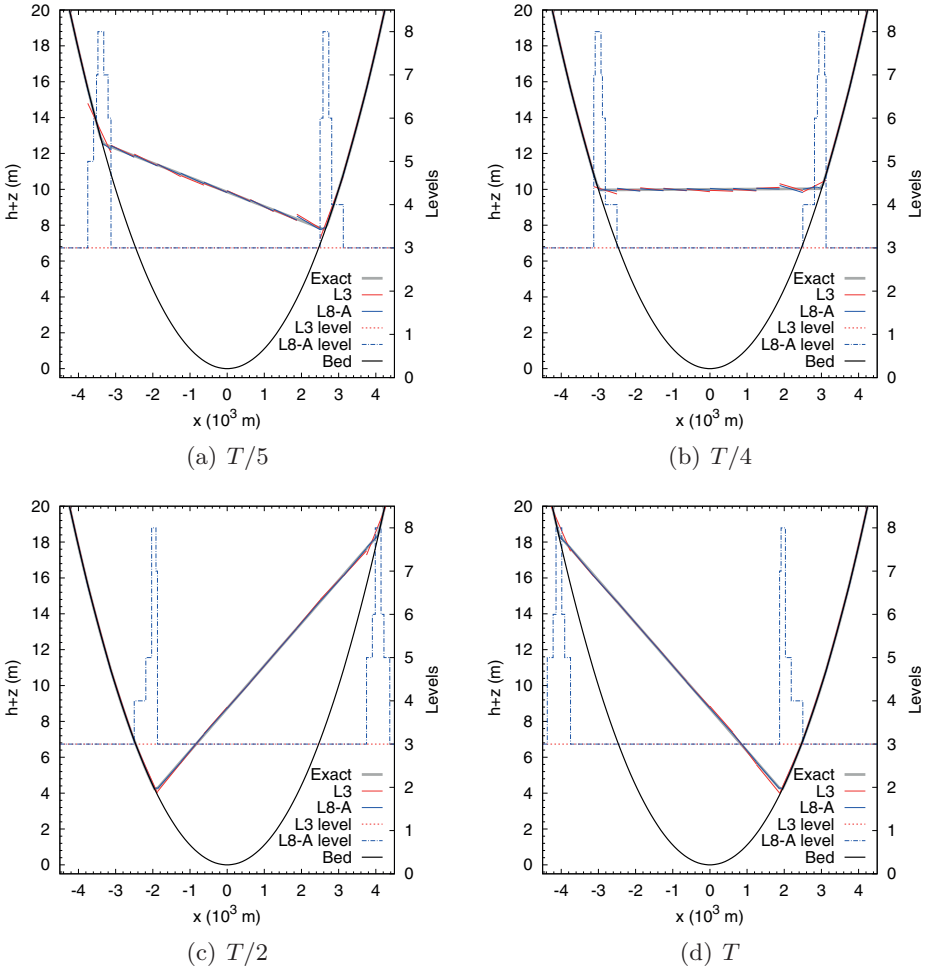

Fig. 10. Comparison of uniform and adaptive water surface results (full solution) with the analytical solution for the parabolic bowl test, along with adaptive resolution levels.

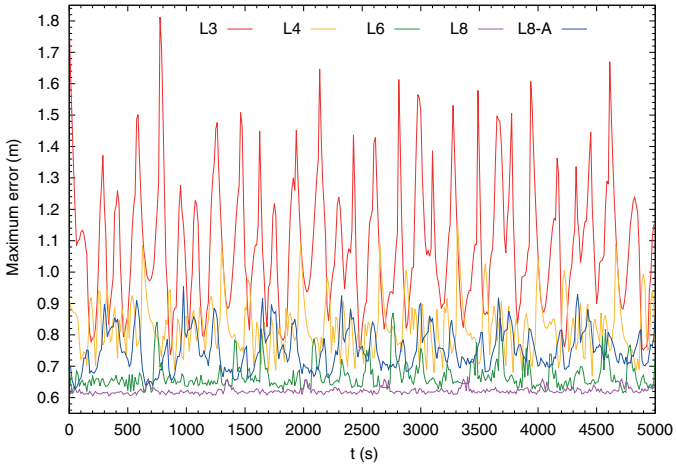

Fig. 11. Comparison of the evolution of the maximum error in the parabolic bowl case for different uniform and adaptive cases.

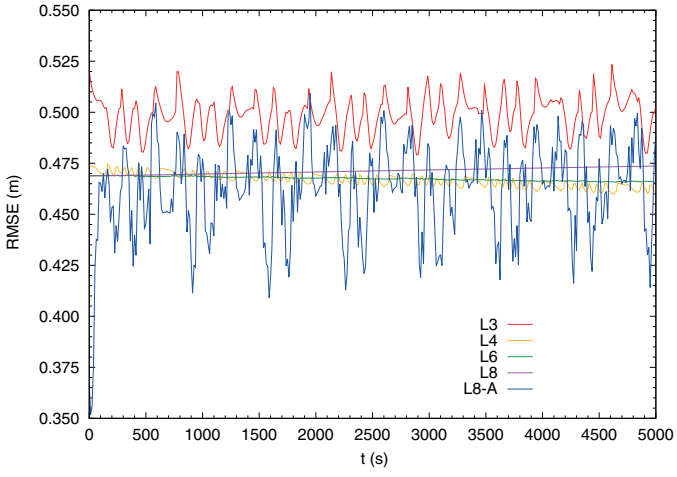

Fig. 12. Comparison of the evolution of RMSE in the parabolic bowl case for different uniform and adaptive cases.

Together, the RMSE and maximum error (infinity norm) allow to better assess the effects of resolution and adaptivity. They clearly show a gain in accuracy as resolution is increased under uniform meshes –as is expected–, but they also quantitatively show the leap that adaptivity provides, specially in terms of the maximum (local) errors that may arise in regions of the flow that require high resolution. The error analysis also shows what can be seen in Fig. 10, i.e., the L3 mesh produces good results on average terms, as evidenced by RMSE, but not in local terms at the wet/dry front, as evidenced by maximum error.

Following this behaviour of the errors around the wet/dry front, which is one of the key issues in this test case, consider Fig. 13 which shows the evolution of the right wet/dry front (i.e., for $x > 0$). The exact solution is shown together with the L3, L8 and L8-A numerical

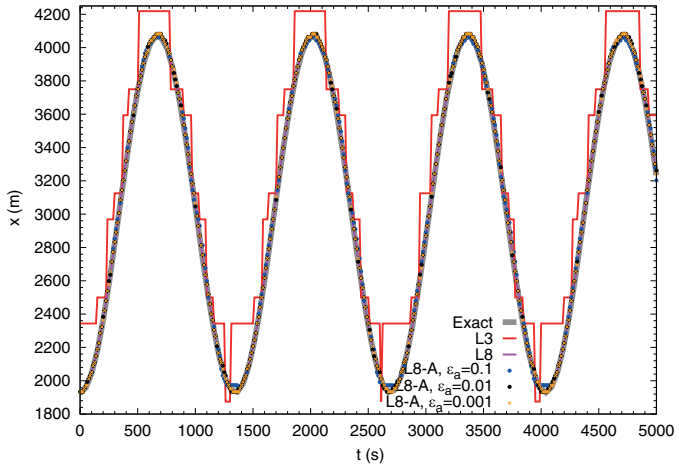

Fig. 13. Comparison of the evolution of the position of the right wet-dry front for the parabolic bowl test, including a coarse and find uniform mesh and three adaptive cases with different threshold values.

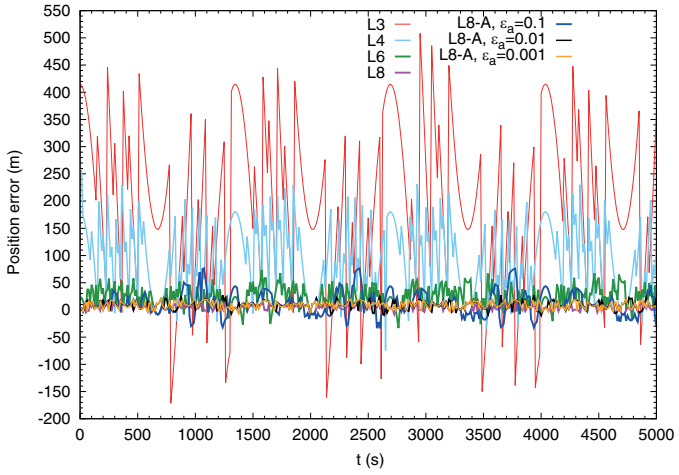

Fig. 14. Comparison of the evolution of wet dry front position error in parabolic bowl for all tested setups.

solutions. To complement and better assess the results, also consider Fig. 14 where the error ε_{wd} in position of the (right-side) wet-dry front is shown, computed as

$$\varepsilon_{wd} = \underline{x}_{wd}(t) - x_{wd}(t) \tag{37}$$

Firstly, note that the L3 wet-dry front approximately tracks the exact front, but has large gaps, specially near inflexion points (that is, around $t = nT/2$). The abrupt changes in the position of the front, and the gaps shown by the L3 solution are clearly due to the coarse resolution $\delta x = 625$ m. It is reasonable that the position of the front can only be approximated coarsely with such resolution. The L8 case tracks accurately the front during the entire simulation. Finally, the L8-A case, in which the wet-dry front is solved at the highest resolution tracks closely the exact solution, with small differences at the inflexion points. The errors shown in Fig. 14 make this very clear. The error in front position for L8-A is comparable to L8. Another remarkable behaviour is that, as Fig. 13 shows, the transition of the front from drying-to-wetting (minimum points in the figure) seems to be more difficult to reproduce numerically than the wetting-to-drying transition (maximum points). This is likely to be associated with small spurious waves generated at the wet-dry front, which in order to suppress, may require improvements to the wet-dry strategy. In summary, the results indicate that, driven by the same threshold value-parameter, the SW-MWRKDG2 method is able to locally simulate wet-dry fronts at the highest resolution available, while efficiently and sensibly allowing for coarser meshes elsewhere.

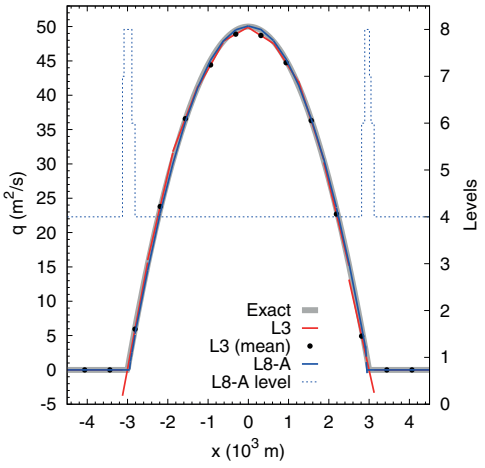

Fig. 15. Comparison of exact and (full polynomial) simulated momentum ($t = T/4$) for uniform and adaptive schemes for the parabolic bowl case. $\epsilon_a = 0.01$.

The choice of the threshold value should be based on the allowable error for the flow feature of interest. In this case, it is the wet-dry front. However, a priori, the magnitude of the threshold value is not clear. To explore what the effects of different threshold values are, additional computations were performed with $\epsilon_a = 0.01$ and $\epsilon_a = 0.001$. In general terms, the solution with all three threshold values are similar. Nevertheless, the results on wet-dry front tracking are clearly improved from $\epsilon_a = 0.1$ to $\epsilon_a = 0.01$ in the drying-to-wetting (minimum points in Fig. 13). From $\epsilon_a = 0.01$ to $\epsilon_a = 0.001$ there is little difference. This is clear in Fig. 14, where the error results for $\epsilon_a = 0.01$ and $\epsilon_a = 0.001$ follow closely those of the non-adaptive L8 solution. Average cell number for computations with $\epsilon_a = 0.1$ was 53 cells (10.4% of uniform L8), for $\epsilon_a = 0.01$ it was 81 cells (15.8%) and for $\epsilon_a = 0.001$ it was 140 cells (27.3%). By examining the changes in accuracy and in efficiency, the optimal threshold value should be around $\epsilon_a = 0.01$, since there is little gain in accuracy with $\epsilon_a = 0.001$ but a significant increase in cost. Note, nevertheless, that the adaptive strategy neither introduces nor eliminates the inaccuracies due to wet-dry cell treatment. The adaptive strategy can only alleviate them by increasing resolution at such location and therefore making these errors smaller, or it can make them evident, when a (too) large threshold value is chosen. Additionally, CPU time for the uniform $L8$ case was 27.3 s. For the adaptive $L8 - A$ case with $\epsilon_a = 0.1$ CPU time was 1.5 s, which translates into a speed-up of 18.2. With $\epsilon_a = 0.01$ the speed-up was 11.5 and for $\epsilon_a = 0.001$ it was 7.4. These rather large speed-ups are the result of refining only at the wet-dry front, while keeping all other regions at a coarse level.

Altogether, these results suggest that the wet-dry strategy should be improved in the reference model to enhance its performance, and transparently further improving enhancing the adaptive model both in terms of accuracy and efficiency.

Following the previous discussion on the adaptive threshold, a value of $\epsilon_a = 0.01$ has been chosen to illustrate momentum results. Fig. 15 shows the exact and computed momentum profile at time $t = T/4$ when the curvature of the momentum is maximum. The full polynomial solution is shown. The figure clearly shows that the coarse L3 mesh approximates the exact solution well, with the exception of the wet-dry front where the full polynomial solution overshoots, although the mean values do not. This is relevant, since it shows that the overshooting comes only from the coarse resolution of the L3 case. The adaptive L8-A case accurately reproduces the exact solution, with no overshooting. Note that the adaptive patterns

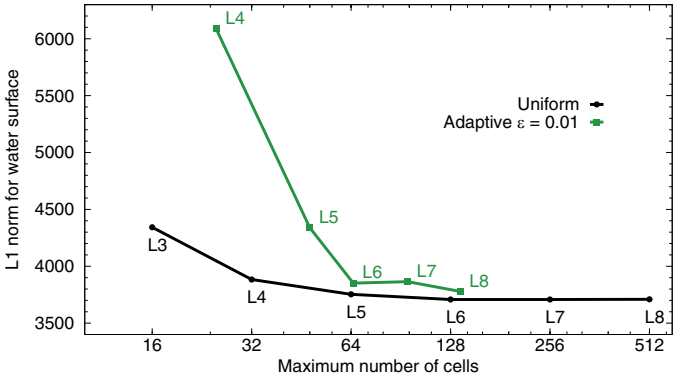

Fig. 16. Mesh convergence results ($t = T/2$) with L1 error norm for uniform and adaptive computations of the parabolic bowl case.

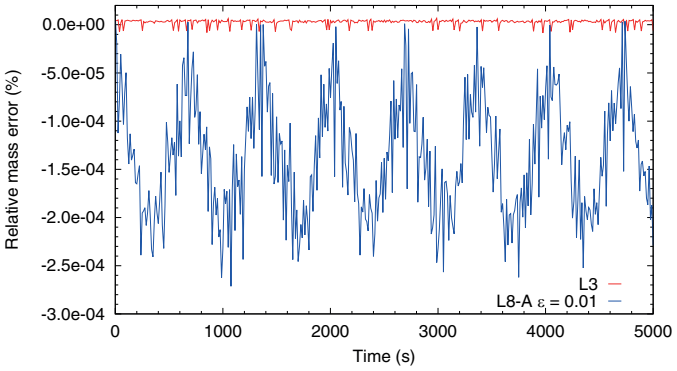

Fig. 17. Relative mass error for a uniform and adaptive solution of the parabolic bowl case.

is slightly different from the one shown in Fig. 10(b) because of the change in the adaptive threshold.

Fig. 16 shows mesh convergence curves for uniform and adaptive computations, also performed using $\epsilon_a = 0.01$, in terms of the L_1 norm defined in Eq. (38) It is worth noting the clear asymptotic behaviour in the uniform case showing that there is little gain in increasing resolution any further. The adaptive computations were all performed with a coarse baseline mesh of $\mathcal{N}_0 = 2$ cells and varying the number of levels. Therefore, the highest resolution in each adaptive case is the same as the corresponding uniform case with the same name. The adaptive solution shows that there is a significant gain between L4 and L6, but there is no real gain afterwards. More importantly, the error for L6, L7 ans L8 is similar to the asymptotic error in the uniform case for L5 through L8. This shows that the approximation error for the adaptive computations is of the same magnitude as the uniform computations, but with significantly less cells. This is consistent with previously reported convergence analysis on this topic [31] for fully wet cases.

$$L_1 = \sum_{i \in \mathcal{M}_\mathcal{A}} |\varepsilon_i| \tag{38}$$

Finally, relative mass error is shown in Fig. 17, where it can be seen that mass error with both the uniform and adaptive achieve a low relative mass error. The mass error in the adaptive scheme is larger than the uniform scheme, which is attributed to truncation and hard thresholding in the adaptive process.

5.4. Experimental dam break flow over triangular obstacle

This test case is an experimental dam-break on a one-dimensional channel with a symmetric triangular obstacle [25]. It is a well-known case which has been previously reported for benchmarking [6,32,42].

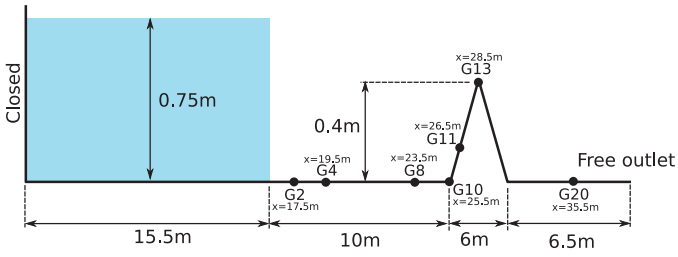

Fig. 18. Experimental dam break over triangle setup and gauge locations.

The purpose of simulating this experimental case is to test the performance of the adaptive strategy in a case which includes realistic features that usable hydraulic models should consider, namely, interacting moving shocks, a non-smooth bed, fast-moving wet-dry fronts and friction. Experimental data was recorded by seven water level gauges, denoted GX (where X is the distance in meters from the initial dam location). The setup is schematically shown in Fig. 18. Manning's coefficient is 0.0125 $\mathrm{m}^{-1/3}\mathrm{s}$. The simulation was run until $t = 90$ s.

The numerical setup is with a baseline mesh with $\mathcal{N}_0 = 2$ cells and $L = 8$. A uniform, non-adaptive solution was computed on an L8 equivalent mesh with $\mathcal{N}_L = 512$.

Fig. 19 shows the experimental and numerical depth time evolution at each gauge. Both uniform and adaptive results are shown. Numerical results reproduce experimental data well, and agree to what has been reported in the literature [6,32,42]. Adaptive and uniform solutions match each other very closely, with no observable differences at the gauges. Fig. 19 also shows the evolution of the resolution level of the cell which (at any time) contains the gauge in the simulation. Cell level evolution has an informative behaviour across all gauges. Fig. 19(d) shows that G10 is the only gauge which does not experience a change in resolution level; instead, it is constantly at level 8. This is because resolution is further governed by the bed at this location which falls exactly at a kink in the bed. At this location, even when under the initially dry conditions the mesh is refined to the highest level. Regardless of flow conditions, the level cannot fall below the level required by the bed, in order to preserve its overall accuracy throughout the simulation. All other gauges show a highly adaptive behaviour. Common to all, is the response to shock arrival. This is clearly observed in Fig. 19(a) for example. Whenever a shock arrives, that location is quickly refined to level 8, and as the shock passes, that location is slowly coarsened down to level 3. Fig. 19(f) shows that at G13, there is a more intense adaptive response. Whenever G13 is wet, the level quickly rises to level 8 and stays at high levels of resolution. Conversely, as soon as it becomes dry, the level immediately drops and remains at level 3. This is even more evident in Fig. 19(g) which shows that at G20, resolution is kept at level 2 for most of the simulation, with the exception of the period during which G20 is wet, where it requires level 3 or 4. Furthermore, the arrival of the wave and the wetting front trigger an immediate refinement to level 8, which has a very short duration. This overall behaviour clearly demonstrates how the multiresolution adaptive strategy can inherently cope with the complex features of the flow, namely moving shocks, moving wet-dry fronts and capturing their arrival times.

Fig. 20 shows water surface profiles at different times. Both numerical solutions are shown, as well as the corresponding cell level profile. Cell edges are marked with a dot on the bed for a visual reference of cell sizes. The profiles allow to observe the spatial distribution of resolution, in response to flow and bed features. Initially (Fig. 20(a)), the discontinuity in water elevation and the kinks in the bed are refined to the highest level. The shock wave is tracked at level 8 as shown at all times in Fig. 20. The wet-dry front is also tracked at level 8 as shown in Figs. 20(b), (e) and (f). It is worth discussing the small oscillations trailing the shock. These are due to the chosen limiting strategy, which allows tiny oscillations around the shock,

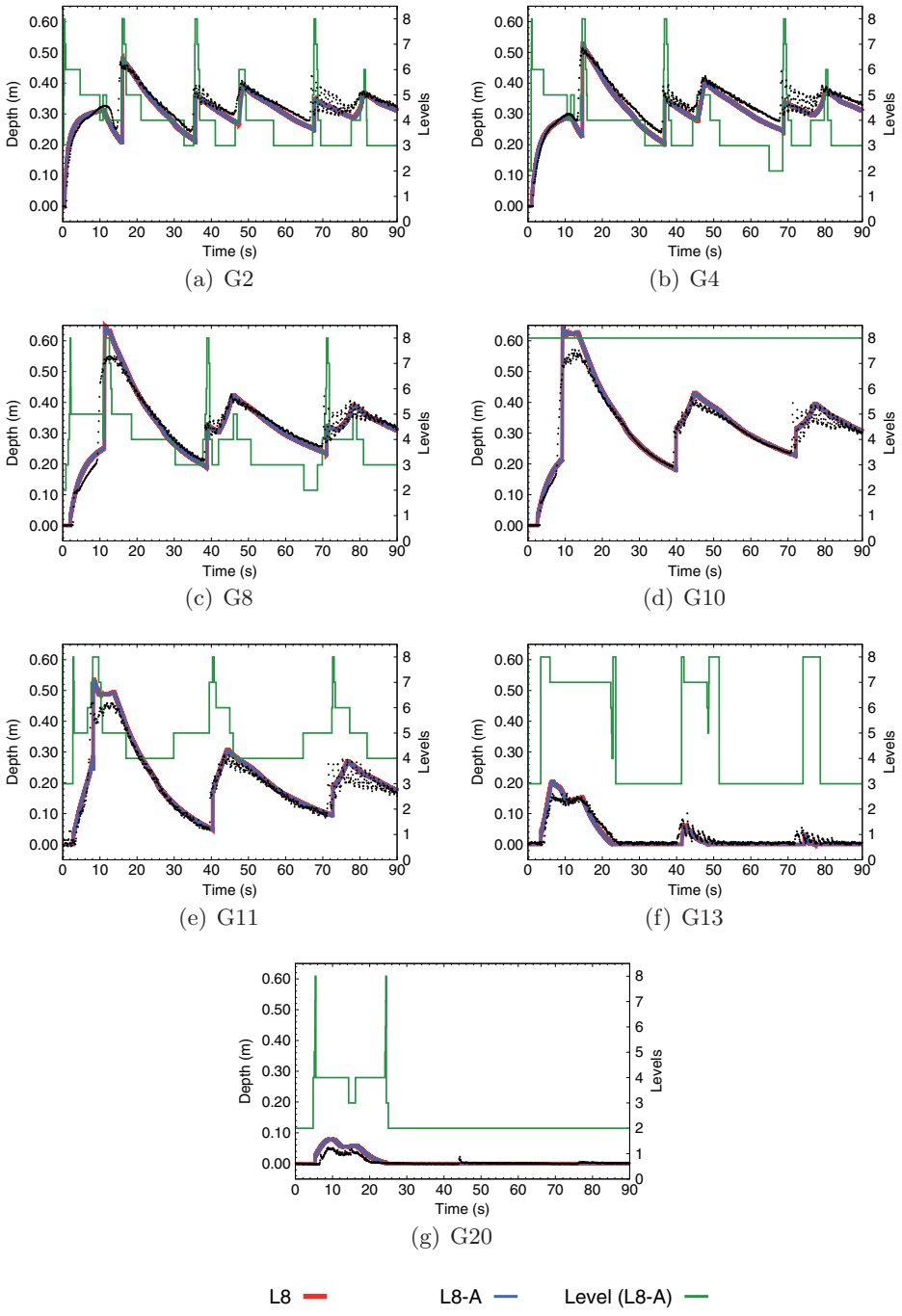

Fig. 19. Depth and refinement level evolution at experimental gauges for the experimental test.

in order to avoid unnecessary limiting in smoother regions [55] depending on the choice of the discontinuity detector threshold value $\epsilon_{\hat{\delta}}$. Note that it happens both in the non-adaptive and the adaptive results, which is evidence that it is not introduced by the adaptive scheme. However, the adaptive scheme presents the added issue that these oscillations can generate significant details, therefore triggering the adaptive process to attempt to track these (artificially and unnecessarily) complex features of the solution, thus slightly over-refining around the region which trails the shock. The response of the adaptive scheme to these spurious perturbations is controlled by the threshold value ϵ_a, which in this particular case is chosen already rather large, to achieve high efficiency. To alleviate the effects of these spurious perturbations $\epsilon_{\hat{\delta}} < 1$ could be set to increase the activity of the slope limiter, while keeping $\epsilon_a \geq 0.1$ in order to lessen the sensitivity of the adaptive process. Nonetheless, it would be preferable, in order to optimise the adaptive solution, to avoid generating such perturbations in the reference scheme. Even so, as shown in the results, the adaptive solution is as accurate as the uniform solution. Moreover, if limiting in the non-adaptive scheme is improved, the adaptive scheme will consequently improve as well, not only in accuracy but also in efficiency.

Fig. 21 shows the evolution of the number of cells in the adaptive case, as a percentage of the (constant) number of cells in the non-adaptive case $\mathcal{N}_L = 512$. From the figure it is clear that the adaptive solution with $\epsilon_a = 0.1$ requires no more than 22% of the cells that the uniform scheme used. The adaptive solution required a minimum of 9.6% of the uniform cell number, and on average 13.9%. For the sake of comparison, results for smaller threshold values ($\epsilon_a = 0.01$

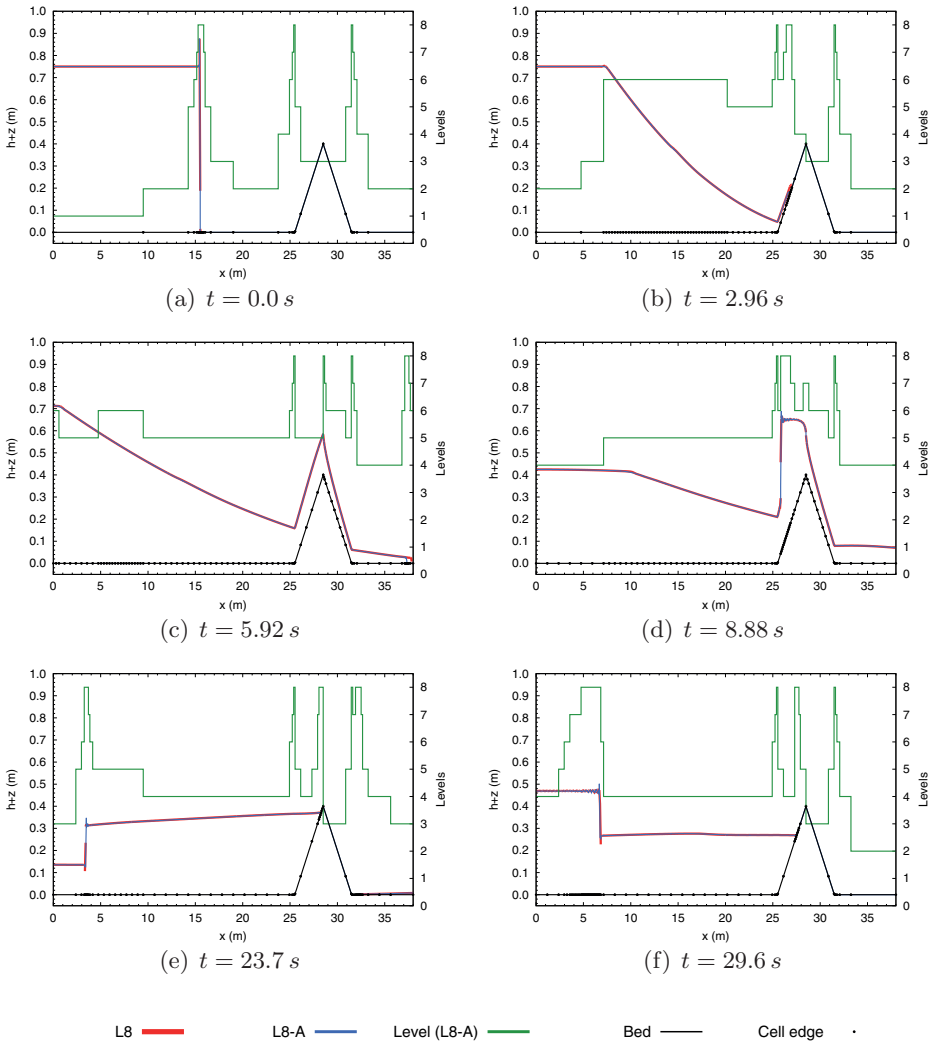

Fig. 20. Evolution of water surface profiles and adaptive mesh refinement for the experimental test case.

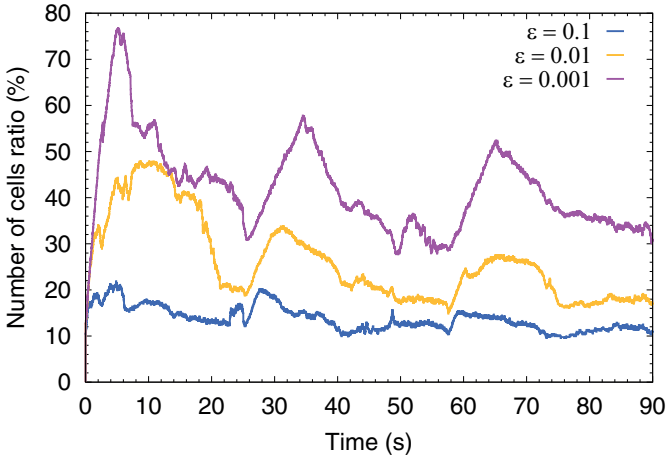

Fig. 21. Comparison of the evolution of number of cells for three adaptive threshold values in the experimental test.

and $\epsilon_a = 0.001$) are included. Depth evolution and depth profiles are similar with all threshold values (and therefore are omitted for clarity in Figs. 19 and 20). However, as seen in Fig. 21, the number of cells clearly varies with changes in the order of magnitude of the threshold value. As is expected, the smaller threshold value $\epsilon_a = 0.001$ generates the most cells during the simulation, because small perturbations in the wet-dry front and around the shock are preserved. Conversely, these small perturbations are filtered out by larger threshold values. These small perturbations originate from standing issues in the reference (non-adaptive) scheme, but can clearly decrease the efficiency of the adaptive scheme. It is expected that, by further improving the reference scheme, such small perturbations may be avoided. Moreover, this would lead to the adaptive response, with different threshold values, to show less dispersion, since adaptivity will respond only to physical variations. This remains to be investigated, but opens the need to further adopt and build upon the latest techniques in computational hydraulics to further optimise the response of the adaptive scheme.

CPU time for uniform mesh computations was 130.8 s. Adaptive computations for $\epsilon_a = 0.1$ achieved a speed up of 7.0, for $\epsilon_a = 0.01$ the speed up was 1.8 and for $\epsilon_a = 0.001$, it was 2.1. In all three cases, the adaptive processes are responsible for approximately 20% of CPU time. The speed-up result for the $\epsilon_a = 0.01$ case are surprising, since it does not follow the expected trend, i.e., lower thresholds require more cells, therefore less speed-up. Such behaviour cannot be explained by cell number, in particular when considering Fig. 21, which shows that at all times the number of cells satisfies the aforementioned trend. In order to explore the cause of this, consider Fig. 22, in which time step evolution for the uniform and all three adaptive

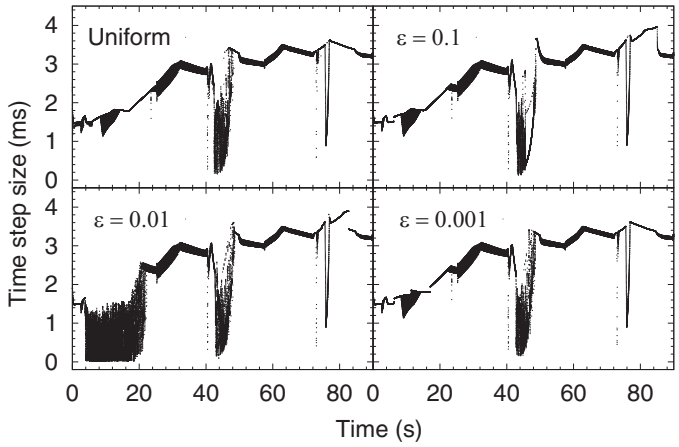

Fig. 22. Comparison of time step size evolution for uniform and three adaptive computations in the experimental test.

cases are shown. Firstly, note that the uniform and the $\epsilon_a = 0.1$ and $\epsilon_a = 0.001$ cases resemble very much, and the smallest time steps are obtained at around $40\,\text{s} \leq t \leq 50\,\text{s}$ in the three cases. This time roughly corresponds to the period on which water is spilling for the second time over the obstacle (see Fig. 19(f)), when flow conditions are strenuous on numerical stability. On the other hand, Fig. 22 shows that the $\epsilon_a = 0.01$ case results in an overall similar time step size evolution, but with a very relevant difference at around $5\,\text{s} \leq t \leq 20\,\text{s}$, a time at which the time steps are very small, in the same order as in $40\,\text{s} \leq t \leq 50\,\text{s}$. Detailed inspection of the results has shown that the thin layer flowing downstream of the obstacle is of similar magnitude to the perturbations of the numerical solution at those points. Therefore, with this particular threshold value, the scheme cannot discriminate between the wet-dry front and the perturbations, resulting in a fast moving train of wet-dry fronts which of course impacts the time step. When the ϵ_a is larger, the perturbations are filtered out, and when it is lower, the perturbations are actually resolved, thus stabilising the computations. Remarkably, aside from the highlighted differences, time step evolution is similar in all four cases, showing that numerical stability is indeed being controlled by cells at the highest resolution level, either by moving shocks or wet-dry fronts at different times.

6. Summary, conclusions and outlook

The combination of MultiWavelets (MW) and the Runge–Kutta discontinuous Galerkin methods (RKDG) has resulted in a new form of adaptive models (MWRKDG). In the framework of an MWRKDG numerical solution, spatial-resolution adaptivity is driven by one user-input parameter, the use of a coarse baseline mesh is straightforward, data connectivity across various resolutions is rigorous, and quantitative control of the perturbation-error from the finest-uniform-mesh (i.e. reference mesh) is feasible [19,20,28]. Despite the recent theoretical development in MWRKDG adaptive methods, this work has provided a first-time exploration of its implications for computational hydraulics. The tailoring and application of a robust MWRKDG2 adaptive model for Shallow Water (SW) modelling has been studied. An MWRKDG2 model has been explored and assessed within the scope of enabling the application of this adaptive-mesh technology to model realistic SW flows. In the context of adaptive SW-MWRKDG2 modelling, a reference RKDG2 scheme is needed on which the solution on the reference mesh is evaluated by the multiresolution analysis, which is referred to as the *reference scheme*. Two RKDG2 schemes have been considered for this purpose. Scheme 1 follows the approach of [36], while Scheme 2 adopts the method in [70]. Both schemes are known to somewhat possess the ability of handling the features of relevance to practical SW modelling (incl. accurate treatment of irregular topographies with wetting and drying). Steady and transient benchmark tests have been used to assess the practical performance of the adaptive SW-MWRKDG2 model in relation to the choice of the reference scheme. For all the test cases, adaptive simulations have been run for a baseline coarse mesh consisting of 2 computational cells and allowing a maximum of 8 refinement levels. The adaptive results have been analysed (qualitatively and quantitatively) comparing with analytical and experimental data, and with the outputs of the reference schemes. When possible, further comparison with a third-order SW-MWRKDG model (SW-MWRKDG3) has been included. Analysis of the present findings offers new insights into the potential strengths and weaknesses of adaptive SW-MWRKDG modelling for real hydraulic problems.

- The quiescent flow test (Section 5.1) clearly illustrates the relevance of choosing an appropriate reference scheme. In conjunction with Scheme 1, the adaptive SW-MWRKDG2 is found to achieve reliable SW modelling (i.e. over non-differentiable topographies with the presence of wet-dry fronts), as the reference (non-adaptive) Scheme 1 did as such. This scheme is therefore favoured for use with the SW-MWRKDG2, and has been employed for all test cases. In contrast, with Scheme 2, well-balancing issues have occurred, which, although are noted to reduce within the associated adaptive MWRKDG2 model, remained quite present in the momentum (discharge) prediction.
- For a steady transcritical flow with shock (Section 5.2), the adaptive SW-MWRKDG2 model has delivered better-resolved capture of the flow transitions than the RKDG2 computations on a uniform mesh with the same number of cells, and at almost the same computational costs. Further comparison with the SW-MWRKDG3 results suggests that the increase in accuracy-order offers coarser-mesh predictions at smooth regions than with the SW-MWRKDG2 model, although it does not seem to improve shock capturing (as expected). This clearly lays out a benefit in further capitalising on the MW scalability to enable both resolution and accuracy adaptivity (*hp*-adaptivity) to improve the efficiency of the SW-MWRKDG approach.
- The oscillatory flow over a parabolic bowl test (Section 5.3) shows an excellent ability of the SW-MWRKDG2 model to achieve (locally and temporarily) highest-resolution tacking of (moving) wet-dry fronts without any additional treatment. However, slightly more reliable predictions of the wetting front are identified, compared to the drying front, which may be caused by the weaker magnitude of the detail coefficients when the front is recessing and by potential shortcomings from the adopted wetting and drying strategy.
- More realistic assessments of the adaptive SW-MWRKDG2 model have been carried out for the experimental dam-break test (Section 5.4), which involved flow transients over a frictional and uneven bed and a shock-refection and wet-dry front movement. Comparisons with experimental data confirm the SW-MWRKDG2 model's adaptivity is able to sensibly track features of shock-, smooth-, topographic- and wet/dry-character (combined), driven entirely by a single threshold-value parameter.

Common to all the tests and simulations (at any particular time), the adaptive SW-MWRKDG2 model has offered (i.e. for a MW's threshold-value parameter of 0.1) very significant gain in computational efficiency; namely by reducing cell number to 20–80% and speed-up runtime to 2–18 times, relative to the RKDG2 scheme on the reference mesh. The results show that the decrease in computational time is case dependent, since a case might require large proportions of fine cells, thus producing a low speed-up, or on the contrary, require only a few high resolution cells, thus resulting in high speed-up. Computational time also showed that there is an overhead for the

adaptive strategy (in its current implementation) at around 20% of the total (adaptive) computational time.

From this study, future research topics to be tackled, which are relevant to widen the range of applicability of the SW-MWRKDG2 solver, are laid out. In terms of 2D extension, although theoretically feasible for scheme 2 [18], is not straightforward with scheme 1 due to its reliance on *bed-continuity* across all interfaces (and at more than 1 points), which is not possible in 2D quadrilateral meshes. This topic requires more in-depth exploration so that the adaptivity gains offered by MWRKDG2 are not compromised by the shortcomings of the reference scheme. Analysis of the trade-off between baseline mesh resolution and number of resolution levels is also worth a particular investigation.

Acknowledgements

The authors earnestly thank Prof. Siegfried Müller and Nils Gerhard from IGPM, RWTH Aachen (Germany) for their collaboration, sharing their code and their invaluable input in the form of discussion and comments. We also thank Dilshad Haleem for all the deep and fruitful discussions on this topic. The authors would like to acknowledge the UK Engineering and Physical Sciences Research Council (EPSRC) for funding this research through grant EP/K031023/1 and through the Pennine Water Group (PWG) Platform Grant EP/I029346/1. We also acknowledge the German Academic Exchange Service (DAAD) for facilitating international collaboration through Visiting Fellowship A-13-72-005.

References

[1] Alpert B, Beylkin G, Gines D, Vozovoi L. Adaptive solution of partial differential equations in multiwavelet bases. J Comput Phys 2002;182:149–90.
[2] Archibald R, Evans KJ, Drake J, White III JB. Multiwavelet discontinuous Galerkin-accelerated Exact Linear Part (ELP) method for the shallow-water equations on the cubed sphere. Mon Weather Rev 2011;139:457–73.
[3] Audusse E, Bouchut F, Bristeau M, Klein R, Perthame B. A fast and stable well-balanced scheme with hydrostatic reconstruction for shallow water flows. SIAM J Sci Comput 2004;25:2050–65.
[4] Brodtkorb AR, Sætra ML, Altinakar M. Efficient shallow water simulations on GPUs: implementation, visualization, verification, and validation. Comput Fluids 2012;55:1–12.
[5] Brufau P, García-Navarro P, Vázquez-Cendón ME. Zero mass error using unsteady wetting–drying conditions in shallow flows over dry irregular topography. Int J Numer Methods in Fluids 2004;45:1047–82.
[6] Brufau P, Vázquez-Cendón ME, García-Navarro P. A numerical model for the flooding and drying of irregular domains. Int J Numer Methods in Fluids 2002;39:247–75.
[7] BTM Group Ltd. TUFLOW-FV June 2015. http://www.tuflow.com/.
[8] Burguete J, García-Navarro P, Murillo J. Friction term discretization and limitation to preserve stability and conservation in the 1d shallow-water model: application to unsteady irrigation and river flow. Int J Numer Methods in Fluids 2008;58:403–25.
[9] Caviedes-Voullième D, García-Navarro P, Murillo J. Influence of mesh structure on 2D full shallow water equations and SCS curve number simulation of rainfall/runoff events. J Hydrol 2012;448-449:39–59.
[10] Cockburn B, Shu CW. The Runge–Kutta discontinuous Galerkin method for conservation laws V: multidimensional systems. J Comput Phys 1998;141:199–224.
[11] Cockburn B, Shu CW. Runge–Kutta discontinuous Galerkin methods for convection-dominated problems. J Sci Comput 2001;16:173–261.
[12] Colella P, Woodward P. The Piecewise Parabolic Method (PPM) for gas-dynamical simulation. J Comput Phys 1984;54:174–201.
[13] Costabile P, Macchione F. Enhancing river model set-up for 2-d dynamic flood modelling. Environ Model Softw 2015;67:89–107.
[14] Donat R, Martí MC, Martínez-Gavara A, Mulet P. Well-balanced adaptive mesh refinement for shallow water flows. J Comput Phys 2014;257, Part A:937–53.
[15] Duran A, Liang Q, Marche F. On the well-balanced numerical discretization of shallow water equations on unstructured meshes. J Comput Phys 2013;235:565–86.
[16] Duran A, Marche F. Recent advances on the discontinuous Galerkin method for shallow water equations with topography source terms. Comput Fluids 2014;101:88–104.
[17] García-Navarro P, Fras A, Villanueva I. Dam-break flow simulation: some results for one-dimensional models of real cases. J Hydrol 1999;216:227–47.
[18] Gerhard N, Caviedes-Voullième D, Müller S, Kesserwani G. Multiwavelet-based grid adaptation with discontinuous Galerkin schemes for shallow water equations. J Comput Phys 2015;301:265–88.
[19] Gerhard N, Iacono F, May G, Müller S, Schäfer R. A high-order discontinuous Galerkin discretization with multiwavelet-based grid adaptation for compressible flows. J Sci Comput 2015;62:25–52.
[20] Gerhard N, Müller S. Adaptive multiresolution discontinuous Galerkin schemes for conservation laws: multi-dimensional case. Comput Appl Math 2014:1–29.
[21] Godunov S. A difference method for numerical calculation of discontinuous solutions of the equations of hydrodynamics. Matematicheskii Sbornik 1959;47:271–306.
[22] Gottlieb S, Shu CW, Tadmor E. Strong stability-preserving high-order time discretization methods. Siam Rev 2001;43:89–112.
[23] Guinot V, Soares-Frazão S. Flux and source term discretization in two-dimensional shallow water models with porosity on unstructured grids. Int J Numer Methods in Fluids 2006;50:309–45.
[24] Harten A. Adaptive multiresolution schemes for shock computation. J Comput Phy 1994;115:319–38.
[25] Hiver J. Adverse-slope and slope (bump). In: Soares-Frazão S, Morris M, Zech Y, editors. Concerted Action on Dam Break Modelling: Objectives, Project Report, Test Cases, Meeting Proceedings. Université Catholique de Louvain, Civil Engineering Department, Hydraulics Division, Louvain-la-Neuve, Belgium; 2000.
[26] Hou J, Liang Q, Simons F, Hinkelmann R. A stable 2d unstructured shallow flow model for simulations of wetting and drying over rough terrains. Comput Fluids 2013;82:132–47.
[27] Hou J, Simons F, Mahgoub M, Hinkelmann R. A robust well-balanced model on unstructured grids for shallow water flows with wetting and drying over complex topography. Comput Methods in Appl Mech Eng 2013;257:126–49.
[28] Hovhannisyan N, Müller S, Schaäfer R. Adaptive multiresolution discontinuous Galerkin schemes for conservation laws. Math Comput 2014;83:113–51.
[29] HydroniaL.L.C. RiverFlow2D. http://www.hydronia.net/two-dimensional-models/riverflow2d-plus/.
[30] Kesserwani G. Topography discretization techniques for Godunov-type shallow water numerical models: a comparative study. J Hydraul Res 2013;51:351–67.
[31] Kesserwani G, Caviedes-Voullième D, Gerhard N, Müller S. Multiwavelet discontinuous Galerkin h-adaptive shallow water model. Comput Methods in Appl Mech Eng 2015;294:56–71.
[32] Kesserwani G, Liang Q. Well-balanced RKDG2 solutions to the shallow water equations over irregular domains with wetting and drying. Comput Fluids 2010;39:2040–50.
[33] Kesserwani G, Liang Q. A conservative high-order discontinuous Galerkin method for the shallow water equations with arbitrary topography. Int J Numer Methods in Eng 2011;86:47–69.
[34] Kesserwani G, Liang Q. Dynamically adaptive grid based discontinuous Galerkin shallow water model. Adv Water Resour 2012;37:23–39.
[35] Kesserwani G, Liang Q. Influence of total-variation-diminishing slope limiting on local discontinuous Galerkin solutions of the shallow water equations. J Hydraul Eng-asce 2012;138:216–22.
[36] Kesserwani G, Liang Q. Locally Limited and Fully Conserved RKDG2 Shallow Water Solutions with Wetting and Drying. J Sci Comput 2012;50:120–44.
[37] Kesserwani G, Wang Y. Discontinuous Galerkin flood model formulation: luxury or necessity? Water Resour Res 2014;50:6522–41.
[38] Krámer T, Józsa J. Solution-adaptivity in modelling complex shallow flows. Computers & Fluids 2007;36:562–77.
[39] Krivodonova L, Xin J, Remacle J, Chevaugeon N, Flaherty J. Shock detection and limiting with discontinuous Ggalerkin methods for hyperbolic conservation laws. Appl Numer Math 2004;48:323–38. Workshop on Innovative Time Integrators for PDEs
[40] Lacasta A, Morales-Hernández M, Murillo J, García-Navarro P. An optimized GPU implementation of a 2D free surface simulation model on unstructured meshes. Ad Eng Softw 2014;78:1–15.
[41] Li G, Caleffi V, Gao J. High-order well-balanced central WENO scheme for pre-balanced shallow water equations. Comput Fluids 2014;99:182–9.
[42] Liang Q, Borthwick AGL. Adaptive quadtree simulation of shallow flows with wet-dry fronts over complex topography. Comput Fluids 2009;38:221–34.
[43] Liang Q, Hou J, Xia X. Contradiction between the c-property and mass conservation in adaptive grid based shallow flow models: cause and solution. Int J Numer Methods in Fluids 2015;78:17–36.
[44] Macdonald I. Analysis and computation of steady open channel flow Ph.d. thesis. University of Reading; 1996.
[45] Mallat SG. A theory for multiresolution signal decomposition - the wavelet representation. IEEE Trans Pattern Anal Mach Intell 1989;11:674–93.
[46] Müller S. Adaptive multiscale schemes for conservation laws. Springer; 2002.
[47] Murillo J, García-Navarro P. Weak solutions for partial differential equations with source terms: application to the shallow water equations. J Comput Phys 2010;229:4327–68.
[48] Murillo J, García-Navarro P. Wave Riemann description of friction terms in unsteady shallow flows: application to water and mud/debris floods. J Comput Phys 2012;231:1963–2001.
[49] Murillo J, García-Navarro P, Burguete J, Brufau P. A conservative 2D model of inundation flow with solute transport over dry bed. Int J Numer Methods in Fluids 2006;52:1059–92.
[50] Murillo J, García-Navarro P, Burguete J, Brufau R. The influence of source terms on stability, accuracy and conservation in two-dimensional shallow flow simulation using triangular finite volumes. Int J Numer Methods in Fluids 2007;54:543–90.
[51] Nemec M, Aftosmis M. Adjoint error estimation and adaptive refinement for embedded-boundary cartesian meshes. In: Proceedings of the 18th AIAA Computational Fluid Dynamics Conference; 2007.

[52] Nikolos I, Delis A. An unstructured node-centered finite volume scheme for shallow water flows with wet/dry fronts over complex topography. Comput Methods in Appl Mech Eng 2009;198:3723–50.
[53] Noelle S, Pankratz N, Puppo G, Natvig JR. Well-balanced finite volume schemes of arbitrary order of accuracy for shallow water flows. J Comput Phys 2006;213:474–99.
[54] Noelle S, Xing Y, Shu CW. High-order well-balanced finite volume WENO schemes for shallow water equation with moving water. J Comput Phys 2007;226:29–58.
[55] Qiu JX, Shu CW. Runge–kutta discontinuous Galerkin method using weno limiters. Siam J Sci Comput 2005;26:907–29.
[56] Remacle JF, Frãzao SS, Li X, Shephard MS. An adaptive discretization of shallow-water equations based on discontinuous Galerkin methods. Int J Numer Methods in Fluids 2006;52:903–23.
[57] Roe P. Approximate Riemann solvers, parameter vectors, and difference schemes. J Comput Phys 1981;43:357–72.
[58] Sampson J. A numerical solution for moving boundary shallow water flow above parabolic bottom topography. In: Mercer G, Roberts A, editors. Proceedings of the 14th Biennial Computational Techniques and Applications Conference, CTAC-2008; 2009. p. C898–911. http://anziamj.austms.org.au/ojs/index.php/ANZIAMJ/article/view/1351. [June 9, 2009].
[59] Sanders BF. High-resolution and non-oscillatory solution of the st. Venant equations in non-rectangular and non-prismatic channels. J Hydraul Res 2001;39:321–30. http://dx.doi.org/10.1080/00221680109499835.
[60] Sanders BF. Integration of a shallow water model with a local time step. J Hydraul Res 2008;46:466–75. http://www.tandfonline.com/doi/pdf/10.3826/jhr.2008.3243
[61] Shelton A. Multi-resolution discontinuous Galerkin method for unsteady compressible flows Ph.d. thesis. Georgia Institute of Technology; 2008.
[62] Sætra ML, Brodtkorb AR, Lie KA. Efficient GPU-implementation of adaptive mesh refinement for the shallow-water equations. J Sci Comput 2015;63:23–48.
[63] Soares-Frazão S, Guinot V. An eigenvector-based linear reconstruction scheme for the shallow-water equations on two-dimensional unstructured meshes. Int J Numer Methods in Fluids 2007;53:23–55.
[64] Tassi PA, Bokhove O, Vionnet CA. Space discontinuous Galerkin method for shallow water flows - kinetic and HLLC flux, and potential vorticity generation. Adv Water Resour 2007;30:998–1015.
[65] Thacker W. Some exact solutions to the nonlinear shallow-water wave equations. J Fluid Mech 1981;107:499–508.
[66] Toro EF, García-Navarro P. Godunov-type methods for free-surface shallow flows: a review. J Hydraul Res 2007;45:736–51. http://dx.doi.org/10.1080/00221686.2007.9521812.
[67] Xing Y, Shu CW. A new approach of high order well-balanced finite volume WENO schemes and discontinuous Galerkin methods for a class of hyperbolic systems with source terms. Commun Comput Phys 2006;1:100–34.
[68] Xing Y, Shu CW. High order well-balanced finite volume WENO schemes and discontinuous Galerkin methods for a class of hyperbolic systems with source terms. J Comput Phys 2006;214:567–98.
[69] Xing Y, Shu CW, Noelle S. On the advantage of well-balanced schemes for moving water equilibria of the shallow water equations. J Sci Comput 2011;48:339–49.
[70] Xing Y, Zhang X, Shu CW. Positivity-preserving high order well-balanced discontinuous Galerkin methods for the shallow water equations. Adv Water Resour 2010;33:1476–93.
[71] Zhou F, Chen G, Huang Y, Yang JZ, Feng H. An adaptive moving finite volume scheme for modeling flood inundation over dry and complex topography. Water Resour Res 2013;49:1914–28.
[72] Zhou J, Causon D, Mingham C, Ingram D. The surface gradient method for the treatment of source terms in the shallow-water equations. J Comput Phys 2001;168:1–25.
[73] Zhu J, Zhong X, Shu CW, Qiu J. Runge–Kutta discontinuous Galerkin method using a new type of WENO limiters on unstructured meshes. J Comput Phys 2013;248:200–20.